A skill assessment of the biogeochemical model REcoM2 coupled to the finite element sea-ice ocean model (FESOM 1.3)

V. Schourup-Kristensen, D. Sidorenko, D. A. Wolf-Gladrow, and C. Völker

Alfred-Wegener-Institut Helmholtz-Zentrum für Polar- und Meeresforschung, Bremerhaven, Germany

Correspondence to: V. Schourup-Kristensen
(Vibe.Schourup-Kristensen@awi.de)

Abstract

In coupled ocean-biogeochemical models, the choice of numerical schemes in the ocean circulation component can have a large influence on the distribution of the biological tracers. Biogeochemical models are traditionally coupled to ocean general circulation models (OGCMs),
5   which are based on dynamical cores employing quasi regular meshes, and therefore utilize limited spatial resolution in a global setting. An alternative approach is to use an unstructured-mesh ocean model, which allows variable mesh resolution. Here, we present initial results of a coupling between the Finite Element Sea-ice Ocean Model (FESOM) and the biogeochemical model REcoM2, with special focus on the Southern Ocean.

10   Surface fields of nutrients, chlorophyll a and net primary production were compared to available data sets with focus on spatial distribution and seasonal cycle. The model produces realistic spatial distributions, especially regarding net primary production and chlorophyll a, whereas the iron concentration becomes too low in the Pacific Ocean. The modelled net primary production is $32.5 \, \mathrm{Pg \, C \, yr^{-1}}$ and the export production $6.1 \, \mathrm{Pg \, C \, yr^{-1}}$, which is lower than satellite-based
15   estimates, mainly due to excessive iron limitation in the Pacific along with too little coastal production. The model performs well in the Southern Ocean, though the assessment here is hindered by the lower availability of observations. The modelled net primary production is $3.1 \, \mathrm{Pg \, C \, yr^{-1}}$ in the Southern Ocean and the export production $1.1 \, \mathrm{Pg \, C \, yr^{-1}}$.

All in all, the combination of a circulation model on an unstructured grid with an ocean
20   biogeochemical model shows similar performance to other models at non-eddy-permitting resolution. It is well suited for studies of the Southern Ocean, but on the global scale deficiencies in the Pacific Ocean would have to be taken into account.

1   Introduction

Primary production plays a large role in ocean carbon cycling, and understanding the drivers
25   behind primary production is therefore of paramount importance when it comes to understanding the changes that a future warmer climate will bring. Observations, as well as coupled

biogeochemical-ocean models, indicate that climate change will decrease the oceanic net primary production (Behrenfeld et al., 2006; Steinacher et al., 2010). This would have far-reaching implications, from changes of the carbon cycle to effects on fisheries.

Coupled biogeochemical-ocean models are important tools used to analyse the net primary production in the ocean and the effects of climate change on it (e.g. Le Quéré et al., 2003; Bopp et al., 2013). The biogeochemical results of such models is highly impacted by the mixing and circulation of the ocean model as it controls processes such as horizontal advection and nutrient supply to the surface layer (Doney et al., 2004). Supply of nutrients through upwelling is especially important when it comes to modelling the equatorial Pacific (Aumont et al., 1999) and the Southern Ocean, where production is iron limited and sensitive to new supply. Results from the 2nd Ocean Carbon-cycle Model Intercomparison Project (OCMIP-2) highlighted the importance of the ocean model; they showed how the representation of the ocean circulation in the Southern Ocean has a large impact on the calculations of present and future uptake of CO_2 (Doney et al., 2004), and reported that the global export production varied between 9 and $28 \, \mathrm{Gt \, C \, yr^{-1}}$ when the same biogeochemical model was coupled to different OGCM's (Najjar et al., 2007).

Traditionally, global OGCMs employ structured grids with relatively uniform spatial resolution in the entire domain, and local refinement is done by utilizing nested models.

The unstructured mesh technology is emerging as an alternative to nesting in ocean models, and is gradually becoming more widespread within the ocean modelling community (e.g., Chen et al., 2003; Danilov et al., 2004; Piggott et al., 2008). As solutions for the global ocean state provided by models formulated on unstructured meshes have improved (e.g., Sidorenko et al., 2011), it has become feasible to exploit the advantages offered by such models in biogeochemical modelling by coupling a biogeochemical model to an unstructured-mesh ocean model (Hill et al., 2014). One may then benefit from the possibility of aligning the grid with the bathymetry, or refining it in areas of interest without the loss of accuracy that the nesting introduces at boundaries. This is especially relevant when it comes to modelling features such as mixed layer depth, upwelling and the presence of fronts and eddies that are of vital importance for realistic modelling of ecosystems.

A drawback of the unstructured mesh technology is that, although computer time is saved by using high resolution in chosen areas only, it still uses a substantial amount of computer time as it is less efficient per degree of freedom as compared to structured models. Furthermore, extra care must be taken for models formulated using the continuous finite elements as their local con-
5   servation of volume and tracers is formulated in the cluster-weighted sense. This brings some ambiguity in analyzing fluxes between grid cells, while divergences are well-defined (Sidorenko et al., 2009).

Before using a newly coupled biogeochemical-ocean model for scientific studies, the skill of the model must be assessed (e.g. Assmann et al., 2010). Performing a skill assessment is not
10 a trivial exercise, considering both the lack of data, especially for parameters such as dissolved iron and export production, and also the inherent uncertainty of the biogeochemical models, in which complex biochemical processes are described by comparably simple mathematical parameterizations. We have coupled the Regulated Ecosystem Model (REcoM2) to the Finite Element Sea-ice Ocean Model (FESOM), and in this paper a skill assessment of the coupled
15 model is carried out with emphasis on the Southern Ocean. We show to what extent the results are comparable to observations and discuss how they compare to results from other models.

2   Method

2.1   Ocean model

The ocean component of FESOM solves the hydrostatic primitive equations under the Boussi-
20 nesq approximations (Danilov et al., 2004; Wang et al., 2008). Elastic Viscous Plastic (EVP) sea ice dynamics is used together with the thermodynamics adopted from Parkinson and Washington (1979) as described in detail by Timmermann et al. (2009). Currently FESOM is used for simulation of the three-dimensional global ocean with special focus on the Arctic and the Antarctic (Haid and Timmermann, 2013; Wekerle et al., 2013). The latest FESOM version is
25 comprehensively described in Wang et al. (2014a).

4

FESOM operates on unstructured meshes what ensures the main feature of the model: the capability of local grid refinement in an otherwise global setup without nesting. The model domain is discretized by a horizontally triangulated and unstructured, but vertically stratified, mesh with tetrahedral volumes. Integration is carried out on an Arakawa A-grid, which uses vertical z coordinates for simplicity. The mesh used in this study (Fig. 1) is similar to the one used by Sidorenko et al. (2011), in which the horizontal resolution ranges from 15 km in the Polar Regions to 180 km in the subtropical gyres. In the vertical it has 32 layers, of which nine are located in the upper 100 m.

The bottom topography of FESOM's grid is constructed using a combination of different data products; the bulk of FESOMS bathymetry, from 60° S to 64° N, is based on topography data from the General Bathymetric Chart of the Oceans (GEBCO, 1 min resolution), south of 60° S, the bottom topography from Timmermann et al. (2010) with a resolution of 1 minute (Rtopo-1) is used and north of 69° N it is based on data from the International Bathymetric Chart of the Arctic Oceans with 2 km resolution (IBCAO, version 2, Jakobsson et al., 2008). Between 64 and 69° N, a combination of the GEBCO and IBCAO data sets is used. FESOM's bottom topography is created using bilinear interpolation, whereupon smoothing is performed to remove grid scale noise. The topography data also defines the coastline using bilinear interpolation from the data to the model's grid points. For further description of the creation of bottom topography for FESOM, please refer to Wang et al. (2014a).

The version of FESOM used here utilizes a linear representation on triangles (in 2D) and tetrahedrals (in 3D) for all model variables. The same is true for the biological tracers, which are treated similar to temperature and salinity. The temporal discretization is implicit for sea surface elevation and a second order Taylor-Galerkin method together with the flux-corrected-transport (FCT) is used for advection-diffusion equations. The forward and backward Euler methods are used for lateral and vertical diffusivities, respectively and the Coriolis force is treated with second order Adams-Bashforth method.

The vertical mixing is calculated using the PP-scheme first described by Pacanowski and Philander (1981) with a background vertical diffusivity of $1 \times 10^{-4} \, \mathrm{m^2 s^{-1}}$ for momentum and $1 \times 10^{-5} \, \mathrm{m^2 s^{-1}}$ for tracers. Redi diffusion (Redi, 1982) and Gent and McWilliams parameteri-

zation of the eddy mixing (Gent and Mcwilliams, 1990) is applied with a critical slope of 0.004.

The skill of FESOM has been assessed within the CORE framework (Griffies et al., 2009; Sidorenko et al., 2011; Downes et al., submitted), where several sea-ice ocean models were forced with the normal year (CORE-I) and interanually varying (CORE-II) atmospheric states (Large and Yeager, 2004, 2009) and results compared. In these assessments, the full flexibility of FESOM's unstructured mesh was not utilized, but the results from FESOM were still within the spread of the other models, and it was consequently concluded that FESOM is capable of simulating the large-scale ocean circulation to a satisfactory degree.

2.2 Biogeochemical model

The Regulated Ecosystem Model 2 (REcoM2) belongs to the class of so-called quota models (Geider et al., 1996, 1998), in which the internal stoichiometry of the phytoplankton cells varies depending on light, temperature and nutrient conditions. Uptake of macronutrients is controlled by internal concentrations as well as the external nutrient concentrations, and the growth depends only on the internal nutrient concentrations (Droop, 1983). Iron uptake is controlled by Michaelis–Menten kinetics.

An overview of the compartments and fluxes in REcoM2 can be seen in Fig. 2.

The model simulates the carbon cycle, including calcium carbonate, as well as the nutrient elements nitrogen, silicon and iron. It has two classes of phytoplankton; nanophytoplankton and diatoms, and additionally describes zooplankton and detritus. The model's carbon chemistry follows the guidelines provided by the Ocean Carbon Model Intercomparison Project (Orr et al., 1999), and the air–sea flux-calculations for CO_2 are performed using the parameterizations suggested by Wanninkhof (1992).

We do not add external sources to the macronutrient pools since the time scale of the runs is short compared to the residence time of the macronutrients in the ocean (Broecker et al., 1982).

Iron has a much shorter residence time (Moore and Braucher, 2008) and is strongly controlled by external sources as well as scavenging.

6

Dissolved iron is taken up and remineralized by phytoplankton, it reacts with ligands and it is scavenged by detritus in the water column (Parekh et al., 2005). New iron is supplied to the ocean by dust and sedimentary input. For dust input, REcoM2 uses monthly averages (Mahowald et al., 2003; Luo et al., 2003), which have been modified to fit better to the observations from Wagener et al. (2008) (Mahowald, personal communication, 2011). The model assumes that 3.5 % of the dust-field consists of iron and that 1.5 % of this iron dissolves when deposited in the surface ocean. This gives a total aeolian input of $2.65 \times 10^9 \, \mathrm{mol\,DFe\,yr^{-1}}$ to the ocean on average.

A flux of iron from the sediment has been added accounting for an input of $2.67 \times 10^8 \, \mathrm{mol\,DFe\,yr^{-1}}$ on average. It is incorporated following Elrod et al. (2004) with the magnitude of the iron concentration released by the sediment being dependent on the rate of carbon remineralization in the sediment.

The model has one zooplankton class, which is the model's highest trophic level. Grazing is calculated by a sigmoidal Holling type 3 model with fixed preferences on both phytoplankton classes (Gentleman et al., 2003).

The sinking speed of detritus increases with depth, from $20 \, \mathrm{m\,day^{-1}}$ at the surface, to $192 \, \mathrm{m\,day^{-1}}$ at 6000 m depth (Kriest and Oschlies, 2008). Sinking detritus is subject to remineralization.

REcoM2 has sediment compartments for nitrogen, silicon, carbon and calcium carbonate, which consist of one layer into which the detritus sinks when reaching the lower-most ocean layer. Remineralization of the sunken material subsequently occurs in the benthos, and the nutrients are returned to the water column in dissolved state.

REcoM1 and 2 have previously been used for large-scale simulations with focus on the Southern Ocean in setups with the MITgcm (Hohn, 2009; Taylor et al., 2013; Hauck et al., 2013), and the purpose of the current coupling between REcoM2 and FESOM is likewise studies of the Southern Ocean.

A full description of the model equations can be found in Appendix A along with lists of parameters used in the current run.

2.3 Model experiment

We present a numerical hindcast experiment with a newly coupled biogeochemical-ocean general circulation model. The run was forced using the CORE-II dataset, which was developed for the use of coupled sea–ice ocean models and gives an interannually varying forcing for the years
5   1949 to 2008 (Large and Yeager, 2009). As focus here is on evaluating the biological surface processes of a newly coupled model, we follow the example of Vichi and Masina (2009) and Yool et al. (2011) and let the coupled model run for a total of 38 years, from 1971 to 2008. The first 33 years are considered spin-up and we present the results for the years 2004 to 2008. Prior to activating the biogeochemical module, the ocean model had been spun up for 300 years,
10   which is sufficient to reach a quasi-equilibrium state (Fig. 8 in Sidorenko et al., 2011). The length of the time step used throughout the run was 1800 s.

In REcoM2, the tracers for dissolved inorganic nitrogen (DIN) and dissolved silicon (DSi) were initialized with values from the Levitus World Ocean Atlas climatology of 2005 (Garcia et al., 2006), and the dissolved inorganic carbon (DIC) and total alkalinity (TA) tracers were
15   initialized with contemporary values from the GLODAP dataset (Key et al., 2004). Due to scarcity of observations for dissolved iron (DFe), the iron field was initialized with an output from the PISCES model (Aumont et al., 2003), which has been modified south of 45° S with mean observed profiles from Tagliabue et al. (2012). All other tracers were initialized with arbitrary small values.

20   We used a constant value for the atmospheric CO_2 during the simulation. Because of the duration of the simulation, the carbon cycle is not in equilibrium at the end of the run, and we do not to focus on this part of the model here.

2.4 Data and skill metrics

The focus of this skill assessment is on the key parameters of the physical, chemical and bi-
25   ological surface fields. We examine the model behaviour on the global scale and in the ocean regions shown in Fig. 3. We have a special interest in the Southern Ocean and therefore also look further into the production and its drivers there.

The performance of the model regarding sea surface temperature (SST), sea surface salinity (SSS), mixed layer depth (MLD), DIN, DSi, chlorophyll a (Chl), net primary production (NPP) and export production (EP), is summarized in Taylor diagrams, one displaying the spatial agreement between the modelled surface multi-year means and the observations, and one also taking the seasonal variations into account. Due to a lack of monthly data, EP is only plotted in the former Taylorplot. The modelled and observed surface climatologies of these same fields, except SST and SSS, have been plotted to show the bias that is not captured by the Taylor-diagrams. SST and SSS were omitted as they have been evaluated elsewhere (Sidorenko et al., 2011). Global climatologies of dissolved iron concentrations do not exist, making it impossible to evaluate the modelled iron fields in the manner described above. Instead, the modelled surface climatology of the iron concentration is plotted on it's own, and mean values of the ocean basins are compared to observation compilations in table form. NPP is the model's end result, and we have therefore additionally plotted the mean seasonal cycle of the NPP for each of the ocean basins defined in figure 3, for the model result as well as satellite-based observations. Due to the large effect the modelled mixed layer has on the prediction of the NPP, we have also chosen to illustrate the seasonal cycle of the modelled and observed mean MLD in these same ocean basins.

A full list of the observations used can be seen in Table 1.

For the net primary production we use the VGPM-product from the ocean productivity webpage (http://www.science.oregonstate.edu/ocean.productivity/index.php), which is based on the SeaWIFS chlorophyll measurements and the VGPM NPP-model (Behrenfeld and Falkowski, 1997). We have downloaded monthly values from the webpage, and from these calculated the spatial and seasonal means. The EP fields from Schlitzer (2004), Siegel et al. (2014) and Laws et al. (2000) were provided as climatologies.

Satellite-based estimates of chlorophyll a, NPP and EP provide detailed spatial and temporal data, but obtaining them is not trivial. Remotely sensed global ocean colour values are first converted to chlorophyll a, and under a number of assumptions about for instance mixed layer depth, temperature and light, NPP (Behrenfeld and Falkowski, 1997) and finally EP (e.g. Laws et al., 2000; Siegel et al., 2014) can be estimated. Increasing uncertainty is introduced during

9

the process, and the satellite-based estimates are not as such observations, but rather another way of modelling the chlorophyll a, NPP and EP. The spread between the different satellite-based estimates of NPP is large. Carr et al. (2006) showed that estimates of the global NPP differed by a factor two between 24 models, with the largest discrepancies occurring in the high-nutrient low-chlorophyll and extreme temperature areas. The SeaWIFS algorithms have further been shown to significantly underestimate chlorophyll a concentrations in the Southern Ocean (Gregg and Casey, 2004), and one must consequently be aware of this when using satellite-based estimates from the Southern Ocean.

The Arctic Ocean is likewise an area in which observations are scarce, and for the seasonal Taylor diagrams the modelled results have consequently been removed in both of the polar regions cases when comparable observational value did not exist. As is the case in the Southern Ocean, it is especially the satellite-based observation of NPP that is affected by this during the winter months. The missing seasonal data has likewise led us to cut the northern basins off at $70°$ N in Fig. 3.

The Taylor diagrams (Taylor, 2001), show the correlation (r), the normalized root mean square error (RMSE) and the normalized standard deviation (SD) between the model results and the observations. The correlation between the model and the observations show whether the two datasets increase and decrease simultaneously, the standard deviations tells us about the magnitude of the changes in the data, but not when these changes occur and the centered root mean square error reflects differences in the overall patterns of the two fields after the bias has been removed. The perfect fit between model and observations will have a correlation and a standard deviation of 1 and a RMSE of 0.

In addition to comparing our results to available observations, we discuss them in relation to those of other biogeochemical models. For Dfe, Chl and NPP we have plotted our bias plots to the scale used by Schneider et al. (2008). They present the results of IPSL model, the MPI model and the NCAR model, providing a range of results to hold our model against. We additionally compare to the results from Assmann et al. (2010), who present the results of another non-traditional ocean model coupled to a biogeochemical model, and to Yool et al. (2011). For the export production, Moore et al. (2004) provided a thorough discussion of the export of par-

ticulate organic matter as well as opal, and our spatial plots of export production is consequently plotted to the scale used by them.

3 Model results

3.1 Physics: Mixed layer depth, salinity and temperature

The fit between the spatial distributions of modelled and observed surface temperature and salinity is very good for both spatial (Fig. 4a) and monthly-spatial fields (Fig. 4b), with the correlations being higher than 0.99 and the normalized standard deviations close to 1 for both fields. As is general practice in ocean-only models (Griffies et al., 2009), FESOM's surface salinity is weakly restored towards the PHC climatology (Steele et al., 2001) with a piston velocity of $20\,\mathrm{m\,yr^{-1}}$.

In both FESOM and the observations (de Boyer Montegut et al., 2004), the mixed layer depth is defined as the depth at which the difference between the potential density at $10\,\mathrm{m}$ depth and the MLD is greater than $0.03\,\mathrm{kg\,m^{-3}}$. The spatial distribution of the mean MLD has a correlation of 0.68 and a normalized standard deviation of 0.85 when compared to the data based estimates (Fig. 4).

The seasonal variability of the MLD leads to entrainment of water with high nutrient concentrations to the surface water during winter, and the maximum depth of the mixed layer during the year ($\mathrm{MLD_{max}}$) is therefore especially important from a biological point of view. Overall, the modelled $\mathrm{MLD_{max}}$ fits well with the observations, but it is generally too shallow in the Southern Ocean (Fig. 5), with the consequence that limiting nutrients are not adequately replenished during winter. This may lead to a too small net primary production in the area as well as a dominance of nanophytoplankton over diatoms, as the former needs a lower iron concentration for production. This will be further discussed in Sect. 3.5.

For the monthly fields, the correlation between the modelled MLD and the observations is above 0.6 and the STD equals 1 (Fig. 4b). We investigate this further by plotting the mean depth of the mixed layer in different ocean regions defined in Fig. 3. All basins have correlations

11

above 0.9, except the North Indian and equatorial basins (Fig. 6), leading us to conclude that the seasonal change in the MLD is well predicted by FESOM.

3.2 Nutrients and nutrient limitation

The annual mean surface distribution of DIN and DSi have correlations between model results
5 and observations of 0.91 and 0.86 respectively (Fig. 4a). In the Southern Ocean, the surface DIN concentrations have a negative bias for DIN (Fig. 7) and a positive for DSi (Fig. 8) when the spatial distribution of modelled and observed values are compared. The DIN concentration additionally becomes too high in the subtropical Pacific Ocean (Fig. 7), something we will later argue happens due to astrong iron limitation in the area.

10 The correlation between model results and observations for the spatial-seasonal distribution of DIN and DSi is close to 0.75 for both fields (Fig. 4b). For both nutrients, the seasonal cycle has the best agreement with the observations in the Polar Regions (Not shown).

Iron has been shown to play a large role as limiting nutrient for phytoplankton in the Southern Ocean as well as the equatorial and subarctic Pacific (Martin et al., 1991) and is therefore a key
15 parameter in the model. We compare the model's surface iron concentration to compilations of observations (Moore and Braucher, 2008; Tagliabue et al., 2012) and to other biogeochemical models (i.e. Schneider et al., 2008). It must be mentioned here that the model is not independent of the observations from Tagliabue et al. (2012) as they are also used for initialization of dissolved iron. But as we only compare surface values, and the residence time of iron in the
20 Southern Ocean is much shorter than the model run, the surface iron concentrations at the end of the model run should not be affected by the initialized values.

The pattern of the surface iron concentration in the Atlantic Ocean (Fig. 9) fits well with the observations in Table 2 as well as with the results from the MPI and NCAR models in Schneider et al. (2008), with relative high concentrations in the Equatorial region fed by the dust plume
25 from the Sahara, and concentrations decreasing towards the poles. The iron concentrations in the IPSL model and Assmann et al. (2010) are somewhat lower in the equatorial and southern part of the Atlantic Ocean than our result.

12

In the Indian Ocean, our surface iron concentrations agree well with the IPSL and NCAR models as well as with the results from Yool et al. (2011), with values higher than 1 nM in the Arabian Sea and falling towards 0.3 nM in the main Indian Ocean. Our values also fit well with the observations in the North Indian Ocean (Table 2), and this, along with the agreement between the models using varying magnitudes of sedimentary iron input, indicates that the coastal upwelling in the Arabian Sea is well captured in these models, and that this upwelling is responsible for the high surface iron concentrations in the area. The lower surface iron concentration in South East Asia is on the other hand evident in all of these models with the exception of the IPSL model, indicating that the sediment source plays a larger role in this area. Here, unfortunately we do not have observations to validate the models. In the Pacific Ocean, our result is closest to the one from Assmann et al. (2010), though they have a higher iron concentration along the North and South American west coast, indicating a stronger coastal upwelling in their ocean model. We have a lower surface iron concentration than all models presented by Schneider et al. (2008), even though they all have low concentrations locally. The observations in Table 2 indicate that all models underestimate the surface iron concentrations in the Pacific, especially in the equatorial region where the upwelling plays the largest role. In the Southern Ocean, Table 2 shows that our surface iron concentration is too low, but the spatial distribution of the surface iron fits well with observed values, with the highest values found in the vicinity of the Antarctic and east of the Patagonian shelf (Tagliabue et al., 2012). This distribution can mainly be attributed to the sediment and dust sources of iron and the seasonal ice coverage impeding iron uptake by phytoplankton near the Antarctic continent. These factors are also responsible for maintaining the relatively high surface iron concentration in the Arctic, which becomes iron limited in the absence of the sediment source of iron. Assmann et al. (2010) and Moore and Braucher (2008) also experienced this, with the latter mentioning that the missing sediment source has a modest impact on productivity and iron concentrations away from the Arctic. In the Southern Ocean, our result agrees the best with the IPSL model, with a relatively high coastal concentration, which then falls towards the north. Both the MPI and NCAR models have relatively constant higher values in the area south of 40° S of around 0.5 and 0.3 nM respectively.

13

The comparison to observations is however hindered by the different definitions of the ocean basins. The value of the north Atlantic from Moore and Braucher (2008) does for instance roughly cover the North Atlantic as well as the North-central Atlantic of our definition (Fig. 3). For the equatorial Pacific, Moore and Braucher (2008) report the value 0.84 nM for the whole
5 ocean, and 0.11 nM for the open ocean, where our value is closer to the latter due to the missing coastal processes in the model.

Nutrient uptake limitation is described by Michaelis–Menten kinetics in the model. The Michaelis–Menten coefficient (MM) is computed as $MM = [Nut]/([Nut] + K_{Nut})$, with $[Nut]$ being the nutrient concentration, and K_{Nut} a nutrient and phytoplankton dependent half satura-
10 tion constant.

To plot the distribution of the mean surface limitation we follow the example of Schneider et al. (2008), where the nutrient with the lowest MM in a given place is seen as limiting and it is assumed that other factors, such as temperature and light, are limiting when all Michaelis–Menten coefficients are above 0.7 (Fig. 10).
15 When looking at the yearly mean, iron limits nutrient uptake for both nanophytoplankton and diatoms up to 45° S and in most of the Pacific. Nanophytoplankton is mainly nitrogen limited in the Atlantic and Indian Ocean, concurring with the result by Assmann et al. (2010), Yool et al. (2011) and the IPSL model in Schneider et al. (2008). For diatoms, silicon is limiting in the Atlantic and Indian Oceans as well as the Arctic, a feature that we only share with Yool et al.
20 (2011).

In the high latitudes, the modelled nanophytoplankton, become light limited during the respective winter months. For the Arctic this is most pronounced in February, where the light limitation reaches down to 45° N in the Atlantic Ocean. For the Southern Ocean, the highest degree of light limitation occurs in August when the area south of 55° S is affected. The higher
25 nutrient demand by diatoms means that they are co-limited by iron and light during winter (Not shown).

14

3.3 Chlorophyll and net primary production

Global net primary production sums up to $32.5\,\mathrm{Pg\,C\,yr^{-1}}$ in the model (Table 3), which is lower than the satellite-based estimate of $47.3\,\mathrm{Pg\,C\,yr^{-1}}$ (SeaWIFS and Behrenfeld and Falkowski, 1997) and also slightly below the estimate range of 35 to $70\,\mathrm{Pg\,C\,yr^{-1}}$ given by Carr et al.
5 (2006), but higher than the modelled values ranging from 23.7 to $30.7\,\mathrm{Pg\,C\,yr^{-1}}$ reported by Schneider et al. (2008).

On a global scale, diatoms account for 25.9 % of all production in the model. In the subtropical gyres we see close to zero percent of NPP from diatoms, whereas it constitutes close to 100 % in the Arctic Ocean (Not shown).

10 The correlations between the spatial distribution of modelled results and satellite data are 0.75 for both chlorophyll a and NPP (Fig. 4a), with the mean surface chlorophyll a concentration being somewhat overestimated as compared to the satellite-based estimates in the high latitudes, while the equatorial regions have too low concentrations (Fig. 11) and the extent of the subtropical gyres is too large. Yool et al. (2011) similarly have a higher equatorial chlorophyll a
15 concentration in the equatorial regions of the Atlantic and Pacific Oceans as compared to our model, but their concentration in the Southern Ocean is even higher than ours. And when we compare to the IPSL-model (Schneider et al., 2008), we again see that our equatorial chlorophyll a concentrations are lower, whereas the concentrations in the North Atlantic and Southern Ocean is fairly similar to our result.

20 The spatial distribution of NPP (Fig. 12), follows the same pattern as chlorophyll a, with low production in the oligotrophic gyres along with a higher production in the temperate regions. Production in the gyres is on the low side compared to the satellite-based estimate (Fig. 13), and as they are known to underestimate production here (Friedrichs et al., 2009), our result is most likely much too low here. An explanation may be that the nanophytoplankton in the model
25 does not represent the smallest phytoplankton classes like prochlorococcus and synechococcus, which are important in the gyres. Even though adaption of the modelled intracellular N : C ratio is possible, this is not enough to increase production here to the level seen in satellite-based estimates.

The missing coastal primary production along the west coast of Africa and South America (Fig. 12) along with a positive temperature bias in the areas (not shown) indicate that the upwelling is too weak here. FESOM has a coastal resolution of 40 km, which is relatively high, but this resolution only covers a narrow path along the coasts, which may not be sufficient for the upwelling zones to be resolved properly, additionally the low resolution further out in the subtropical gyres could play a role. Moreover, the driving force for the upwelling is the coastal winds, and the missing upwelling may partially result from a too low resolution of the atmospheric forcing; higher resolution allows strong surface winds closer to the coast, thereby increasing the strength of the upwelling (Gent et al., 2010).

Another explanation is the missing riverine input of macronutrients, which at least in the case of silicon plays a role locally in places like the Amazonas and the Arctic (Bernard et al., 2011). Yool et al. (2011) deal with the missing riverine nutrient input by restoring the nutrient fields along the coasts, and they do have a larger coastal production in their model, especially along the coast of West Africa, but show that the nutrient restoring only has a small influence on this.

When comparing the mean spatial distribution of NPP with other models, our result is the closest to the NCAR-model presented by Schneider et al. (2008), with a relative high production rate in the North and Equatorial Atlantic as well as the Indian Ocean. Moderate production in the area of the Polar Front in the Southern Ocean is a feature that our model shares with the satellite-based estimate (Fig. 12) and with the NCAR and IPSL models from Schneider et al. (2008). Despite our model's strong iron limitation in the Pacific Ocean, our results fits well with the IPSL model, though we have a smaller production rate in the Southern Pacific.

Taking seasonal variations into account, net primary production and surface chlorophyll a have correlations of 0.66 and 0.57, respectively, when comparing the model and the satellite-based estimate (Fig. 4b), and the normalized standard deviations are equal to 1.47 and 1.94 for chlorophyll a and NPP, respectively. Both are on the same order as the values presented by Doney et al. (2009).

The timing of the seasonal cycle of NPP is well captured in the majority of the ocean regions defined in Fig. 3 (Fig. 13). The Pearson's correlation coefficients (R) range from 0.31 in the equatorial Atlantic to 0.93 in the South Central Atlantic (Fig. 13), with significant correlations

16

in eight of the fourteen basins. In general, the modelled seasonal cycle is closest to the satellite-based estimate between 10 and 45° N and S, where the modelled NPP is low, but the magnitude of the seasonal variations fits well with the satellite-based estimate. This is the case for all basins in the mentioned area, except the North Indian basin.

5   The Southern Ocean stands out as it has a modelled NPP of the same magnitude as the satellite-based estimate, but the spring bloom occurs too early here, compared to the satellite-based estimate. This will be further discussed in Sect. 3.5.

3.4 Export production

The export of organic carbon out of the euphotic zone (EP), is calculated at a reference depth,
10   which in our case is set to the standard $100\,\mathrm{m}$ (e.g. Schneider et al., 2008; Doney et al., 2009). Here, we regard EP as the organic matter that sinks due to the effect of gravity, whereas the total EP also entails the vertical movement of POC by advection and diffusion plus a contribution from semi-labile DOC.

The global export production sums up to $6.1\,\mathrm{Pg\,C\,yr^{-1}}$ in the model (Table 3), close to the
15   satellite-based estimate of $6\,\mathrm{Pg\,C\,yr^{-1}}$ from Siegel et al. (2014). It is also within the range of estimates presented by Dunne et al. (2007), but on the low side and closer to modelled estimates than to estimates based on observations or inverse models.

The modelled EP constitutes 20 % of NPP on a global scale, which is similar to the ratio predicted by Laws et al. (2000). The EP field presented by Laws et al. (2000) is calculated at
20   $100\,\mathrm{m}$ depth and is based on satellite observations of ocean colour, whereas the EP field calculated by Schlitzer (2004) is based on an inverse model and is calculated at $133\,\mathrm{m}$. Comparing to these fields can consequently be argued to be more of a model-model comparison than a model-observation comparison.

The correlation is 0.28 and 0.48, when comparing the spatial distribution of EP in our model
25   to the fields by Schlitzer and Laws et al., respectively (Fig. 4a), indicating that our spatial distribution is closer to the field from Laws et al. (2000), and the normalized standard deviations are 0.90 and 0.60, respectively.

17

The EP fields from Schlitzer (2004) and Laws et al. (2000) both have high export along the Equator, in the upwelling regions and along 45° N and S (Fig. 14a and b). In the Southern Ocean, Schlitzer has a comparably higher export in the Indian and Pacific sector and in the North Atlantic he has less than Laws et al. (2000).

REcoM2 captures the overall pattern with high EP around 45° N and S and along the Equator (Fig. 14c and d), and the elevated EP in the North Atlantic is a feature that REcoM2 shares with the field from Laws et al. (2000). Turning to the differences, our EP is lower in the North Atlantic, slightly low in the gyres and higher south of 45° S when comparing to the field by Laws et al. (2000) (Fig. 14e). Compared to the climatology presented by Schlitzer (Fig. 14b), our EP is generally lower in the Pacific and in the upwelling regions along West Africa and America, whereas it is higher in the North and South Atlantic (Fig. 14f). In the Southern Ocean, the differences between the fields are especially visible in the Indian and Pacific sectors; where Laws et al. have very low export, Schlitzer has a rather high export and REcoM2's export lies in between the two. Schlitzer argues that the satellites do not capture the deep blooms that occur in the area, thereby explaining the lack of EP in the satellite-based estimate.

Both the spatial distribution and magnitude of EP in our model is very similar to what was found by Moore et al. (2004).

Vertical export of opal is similarly calculated across a reference depth of $100\,\mathrm{m}$. On a global scale we have a total opal export of $74.5\,\mathrm{Tmol\,yr^{-1}}$. Previous estimates of global export of opal vary widely (Table 3), and our value is in the lower end of the estimates, as are our global values for NPP and EP.

3.5 The Southern Ocean

The coupled model FESOM-REcoM2 is, as a first step, planned to be used for studies regarding biogeochemical processes in the Southern Ocean south of 50° S, and we are therefore especially interested in its performance here. The reasons for this focus are further discussed in section 4.

The model's surface salinity and temperature as well as the nutrient fields are well represented in the spatial domain of the Southern Ocean, with all of them having correlation coefficients above 0.9 when compared to observations (Fig. 15). The chlorophyll a and NPP fields both

have somewhat lower correlations with the correlation for NPP equalling 0.75 and the one for chlorophyll a equal to 0.48.

For the MLD, the correlation between the model results and the observational based estimate (de Boyer Montegut et al., 2004) is 0.63 in the Southern Ocean (Fig. 15). The MLD_{max} is too shallow in the Indian and Pacific sections of the Southern Ocean, especially in the area of the polar front (Fig. 5), causing this low value. In addition to this, FESOM simulates a too deep MLD_{max} in the convection area of the Weddell Sea associated with deep-water formation. This is a common feature in sea-ice ocean models (e.g. Griffies et al., 2009) and should in itself not have a large impact on the production in the Southern Ocean.

The modelled NPP south of $50°$ S sums up to $3.1 \, Pg \, C \, yr^{-1}$ (Table 3). Carr et al. (2006) summarize previous studies of NPP based on ocean colour and report an average NPP of $2.6 \, Pg \, C \, yr^{-1}$ for the Southern Ocean. They also show that the largest uncertainties in satellite-based estimates regarding NPP are found in the Southern Ocean and that biogeochemical models generally predict higher NPP in the area than satellites.

The model's export production equals $1.1 \, Pg \, C \, yr^{-1}$ in the Southern Ocean, close to the $1 \, Pg \, C \, yr^{-1}$ found by both Schlitzer (2002) and Nevison et al. (2012), and the EP : NPP ratio equals 36 % in the Southern Ocean, similar to what was found by Nevison et al. (2012).

Considering the spatial distribution of EP in the Southern Ocean (Fig. 14), the model is closer to the estimate from Laws et al. (2000) with the highest export fluxes occurring in the northern part of the Atlantic and East Indian sectors of the Southern Ocean. REcoM2 does however have a larger EP closer to the Antarctic.

The fraction of the the total biomass comprised by diatoms in the Southern Ocean defers between studies (Alvain et al., 2005; Hirata et al., 2011). In the present study, the diatoms are responsible for 25 % of the NPP south of $50°$ S, varying from 0 % in the very iron limited waters of the South Pacific to 100 % in the iron replete regions of the Weddell Sea and on the Patagonian shelf (Fig. 16). Vogt et al. (2013) compared the results of four ecosystem models and showed that the percentage of diatom biomass in the Southern Ocean differed significantly between them, ranging from 20 to 100 %. Our diatom percentage is accordingly within the spread of other models.

19

Production of the silicon-containing diatoms creates a sinking flux of biogenic silica, which sums up to $21.5\,\mathrm{Tmol\,Si\,yr^{-1}}$ south of $50°\,\mathrm{S}$ in the model (Table 3), which is close to the satellite-based estimate of $25 \pm 4\,\mathrm{Tmol\,Si\,yr^{-1}}$ calculated south of $45°\,\mathrm{S}$ (Dunne et al., 2007), but estimates vary significantly between studies (e.g. Moore et al., 2004; Jin et al., 2006; Holzer

5 et al., 2014).

In REcoM2, the opal export in the Southern Ocean accounts for 29 % of the global opal export (Table 3). This number similarly varies widely between studies, with ours being lower than the 70 % suggested by Jin et al. (2006) and Holzer et al. (2014), but considering the area of the Southern Ocean, its contribution to the global opal flux is still large in our model.

10 High export fluxes of biogenic silica (Fig. 17) naturally occur in places with corresponding high percentage of diatom production (Fig. 16). The largest values are found in the temporary ice zone between 60 and 70° S, as well as in the area east of Patagonia (Fig. ??b), where dust and sediments supply iron to the surface water. A band of relatively high opal export is also present in the polar front in the Atlantic and Indian sectors of the Southern Ocean (Fig. 17).In most of

15 the Southern Ocean, the modelled opal flux falls within a range from 0.4 to $2.5\,\mathrm{mol\,Si\,m^{-2}\,yr^{-1}}$. This is slightly higher than the values given by Moore et al. (2004) and lower than the values of up to $9\,\mathrm{mol\,Si\,m^{-2}\,yr^{-1}}$ in (Jin et al., 2006).

The absence of diatom production in the Pacific sector of the Southern Ocean (Fig. 16), leading to a low opal export in the area (Fig. 17) is notable, and can be explained by the pronounced

20 iron limitation of the Pacific, which also reaches into the Southern Ocean and limits production here.

Control of bloom in the Southern Ocean

We will now examine the roles of MLD and iron concentration in explaining the seasonal variability of NPP. For this purpose we define R^{2*} as the temporal coefficient of determination mul-

25 tiplied by the sign of the regression slope. R^{2*} is calculated for each spatial point in the domain south of $30°\,\mathrm{S}$ between NPP and the MLD (Fig. 18a) and between NPP and DFe (Fig. 18b), using the average iron concentration over the top $100\,\mathrm{m}$ of the ocean. The R^{2*} values show that

the Southern Ocean is roughly divided into two zonal bands; one north of 60° S, in the area of the Polar Front (Moore et al., 1999), and one south of 60° S (Fig. 18).

The general picture north of 60° S is that the concentration of dissolved iron and the mixed layer depth both correlate positively with NPP (Fig. 18), indicating that production in the area mainly is iron controlled, and that production starts when the mixed layer deepens and brings iron and other nutrients to the surface. For the mean seasonal cycle of MLD and NPP north of 60° S (Fig. 19a), the magnitude of the modelled bloom fits nicely with the one from the satellite-based estimate, but the maximum occurs two months earlier. The mean MLD is well predicted by FESOM in the area (Fig. 19a), but it is consistently shallower than what is observed. This has the effect that the modelled phytoplankton receives a larger light intensity than what is the case in the ocean, something that may affect the timing of the bloom. The mean iron concentration in the surface water is highly correlated with the depth of the mixed layer north of 60° S (Fig. 20a). The phytoplankton concentration starts increasing in July, when the iron concentration is high, and reaches a maximum in October, after which a combination of high grazer concentration and decreasing iron concentrations most likely causes the bloom to decline. Under nutrient and light replete conditions, the increase in biomass is a result of the balance between phytoplankton's maximum growth rate and the grazing (Behrenfeld, 2010; Hashioka et al., 2013). This indicates that the model's timing of the bloom on the one side could be changed by a smaller maximum growth rate, something that would change the phytoplankton dynamics on a global scale. On the other side, the modelled zooplankton concentration is tightly coupled to the increase in phytoplankton concentration (Fig. 20a), and increasing the maximum grazing rate is another way of keeping the growth in biomass down. As modelled grazers are set to prefer nanophytoplankton over diatoms, this may further increase the diatom percentage in the Southern Ocean (Hashioka et al., 2013).

The NPP and MLD fields are negatively correlated south of 60° S, whereas correlation between NPP and DFe is close to zero here (Fig. 18). This indicates that light is the main limiting factor in this area and that iron is less important as a controlling factor. The intensity of the incoming light decreases with latitude, and is further decreased or blocked by the presence of sea-ice during parts of the year south of 60° S. The role of the sea-ice for the timing of the

21

spring bloom was highlighted by Taylor et al. (2013), who argued that the sea-ice melting induces a shallower and more stable mixed layer, increasing the average light intensity received by the phytoplankton, thereby instigating growth. In our study, the modelled bloom is larger than what is estimated by the satellites south of 60° S, but the timing fits well (Fig. 19b). The
5 difference can be explained by the aforementioned underestimation of NPP by the satellites, and that the modelled mean MLD is very similar to the observed values. NPP starts increasing when the iron concentration is high and decreasing again when the iron concentration is low and the grazer concentration high (Fig. 20b).

It is worth noticing that the increase in production begins at the correct time in both areas,
10 but that the rate of biomass increase is too high.

The sparse observations make it difficult to assess the validity of the modelled seasonal cycles of iron and zooplankton. Tagliabue et al. (2012) presented a seasonal cycle of DFe from the SR3 transect south of Tasmania. Their results indicate that the highest iron concentrations occur in January and February suggesting that our seasonal change in iron concentration, which peaks
15 in September, is off. Our results do however fit well with the model result from Hoppema et al. (2003), who also see a peak in the iron concentration in September.

4 Discussion and outlook

We have presented a skill assessment of an initial coupling between the biogeochemical REcoM2 and the finite element sea-ice ocean model (FESOM). FESOM's capability of locally
20 increased resolution has not been fully utilized in the current study, with the smallest distance between neighboring gridpoints being only a factor of about 10 smaller than the largest, and as most biogeochemical models (e.g. Yool et al., 2011) we do not resolve eddies. The model run presented here can thus be regarded as a baseline run, from which future work that further explores the capabilities of the new coupling can proceed.

25 Using the current resolution, the advantage of the new FESOM-REcoM2 coupling over the older MITgcm-REcoM2 coupling is not obvious, especially taking FESOM's larger demand for computer time into account. The strength of the new coupling will become clearer when new

studies on specialized meshes have been carried out. We are currently looking into the effect of the ocean model on the biogeochemistry of the Southern Ocean by comparing two model runs between which only the ocean model differs. We assess the differences of the supply of iron to the surface mixed layer from below, and how it affects the NPP in the area (Schourup-Kristensen et al., in prep.).

In regional models of the Southern Ocean, fixed boundary conditions must be added along the northern boundary where the Southern Ocean is connected to the Atlantic, Indian and Pacific Oceans, introducing and extra potential for error in such models. Running the model in a global configuration has the advantage that the boundary conditions can be omitted.

As the dynamics of the iron supply is something we plan to study further in the future, and it is a feature we would like to improve, especially in the Pacific Ocean, we will now discuss how changes to the iron cycle may change the results of the model.

In the Southern Ocean, the spatial distribution of iron in the model is reasonable, but it tends towards low values (Table 2), something that may be explained by the crudely constrained external iron sources in the area. The strength of the sediment source varies widely between models (e.g. Moore and Braucher, 2008; Aumont and Bopp, 2006), and in REcoM2 we have an input of iron from the dust and the sediment source, which is in the smaller end of the range. Increasing the strength of the sediment source would especially impact the iron concentration in the Southern Ocean, but though it has been shown that iron from the sediments can be carried far from the source region (Lam and Bishop, 2008), it would still mainly affect the ocean locally; the Atlantic sector of the Southern Ocean would have an especially large input due to the presence of the Patagonian shelf and the Antarctic Peninsula (e.g. Lancelot et al., 2009), but it would most likely not change the supply to the pelagic areas in the Indian and Pacific Southern Ocean substantially. It would be especially important for the iron limited areas, such as the Southern and the Pacific Ocean to further explore the influence of the aeolian and sedimentary iron sources, as well as the input from ice in the Polar areas.

In the remote parts of the Southern Ocean, the input of iron to the mixed layer from below plays a large role (De Baar et al., 1995; Löscher et al., 1997), and Tagliabue et al. (2014) showed that the entrainment of iron during deepening of the mixed layer was especially important.

23

FESOM's MLD$_{max}$ is too shallow in the Southern Ocean, especially in the region of the polar front in the Indian and Pacific sectors (Fig. 5), something likely affecting the degree of iron limitation in these two areas. The tight coupling between iron concentrations, NPP and MLD in the polar frontal area (Fig. 20a), further confirms the importance of entrainment as a supply mechanism of iron.

The lower iron input favors the smaller nanophytoplankton, which have a lower iron half saturation constant, and thereby a lower requirement for iron. A larger input of iron would probably change the species composition towards more diatoms, but would not necessarily increase primary production (e.g. Wang et al., 2014b). A higher percentage of diatoms would also possibly decrease the models surface silicon concentration, which tends towards high values in the Southern Ocean (Fig. 8). The effect on the silicon concentration is however complicated by the fact that the model's carbon and silicate cycles are decoupled under iron limitation, leading to a higher silicate uptake when the phytoplankton is iron stressed (Hohn, 2009).

In the Pacific Ocean, the surface iron concentration is very low (Fig. 9), inducing iron limitation (Fig. 10), which leads to a build-up of DIN in the surface water (Fig. 7) and low NPP (Fig. 12). The external input of iron from dust and sediment in the model is marginal in the equatorial and southern part of the Pacific and input from upwelling is consequently important here. FESOM produces a reasonable upwelling of 40 Sv along the Equator (Johnson et al., 2001), whereas upwelling is small along the west coast of South America. We have a low iron flux in the upwelled water along the equatorial Pacific in our model ($\sim 10\,\mu\mathrm{mol\,m^{-2}\,yr^{-1}}$) compared to the values suggested by Gordon et al. (1997) and Aumont et al. (2003), who reported 44 and 68 $\mu\mathrm{mol\,m^{-2}\,yr^{-1}}$ respectively. Our result is however higher than the 5.1 $\mu\mathrm{mol\,m^{-2}\,yr^{-1}}$ suggested by Fung et al. (2000). The Fe : C ratio in the upwelled water in the equatorial area is $0.0015\,\mu\mathrm{mol\,Fe\,mmol\,C^{-1}}$ ($6.66 \times 10^6\,\mathrm{mmol\,C\,mmol\,Fe^{-1}}$), which is significantly lower than the prescribed constant intracellular ratio of $0.005\,\mu\mathrm{mol\,Fe\,mmol\,C^{-1}}$ ($2 \times 10^6\,\mathrm{mmol\,C\,mmol\,Fe^{-1}}$) in the modelled phytoplankton. The upwelled water consequently contains too little Fe to sustain growth, explaining why biological production is not able to utilize the upwelled DIN.

Allowing the model's phytoplankton to adapt to the conditions in the water with a varying intracellular Fe : C ratio would be a possible way to increase production, as the ratio would

24

then decrease in areas with low iron concentrations. Variable intracellular Fe : C stoichiometry, as found by Sunda and Huntsman (1995) and Wilhelm et al. (2013), is used in other models (e.g. Moore et al., 2002; Aumont and Bopp, 2006). The intracellular Fe : C ratio in diatoms ranged from $0.002\,\mu mol\,Fe\,mmol\,C^{-2}$ in the equatorial Pacific to $0.007\,\mu mol\,Fe\,mmol\,C^{-2}$ in the subtropical gyres in Moore et al. (2002) and the former value fits remarkably well with our Fe : C ratio in the upwelled water in the Pacific. A lower intracellular Fe:C ratio in our model would lower the intracellular Fe:N ratio and bring it closer to the observed nutrient ratio in the upwelled water, indicating that implementing varying ratios would indeed improve the model's performance in the Pacific.

Other features that could potentially improve the iron cycle are spatially varying solubility of iron in the water, spatially varying ligand concentration and scavenging of iron onto dust particles in the water. The latter is present in the iron cycle used by Moore and Braucher (2008) and would likely counter the relatively high iron concentrations in the equatorial Atlantic and Indian Ocean that are present in our model (Fig. 9).

5 Conclusions

In the current study we show that the newly coupled model REcoM2-FESOM reproduces the large scale productivity and surface nutrient patterns, with the main deficiency being the strongly iron limited Pacific Ocean. The total NPP and EP are within the range of previous estimates, but in the lower end, mainly due to the low productivity in the Pacific. The ratio between EP and NPP is 20 %, similar to the result from Laws et al. (2000).

In the Southern Ocean, the modelled spatial mean fields are likewise reasonable, though the comparison here is hindered by the scarcity of observed data. South of 50° S, the total NPP and EP agrees well with previous estimates, as does the EP to NPP ratio of 36 %. Production is iron and light limited in the Southern Ocean making the external input of iron important as a controller of production.

On a global scale, the model provides reasonable seasonal variations of the net primary production, but the main deficiency in the Southern Ocean is the early onset of the spring bloom in the area between 40 and 60° S.

Overall, the model results at the present resolution are comparable to those of other non eddy resolving biogeochemical models and it is well suited for studies of surface processes in the Southern Ocean on a time scale similar to the one used here.

Appendix A

Equations

In biogeochemical models, the biological state variables are subject to change by the ocean circulation through advection and turbulent mixing as well as by biological processes. Detritus further sinks vertically through the water column due to gravity, and exchange occurs across the surface and bottom boundaries for certain variables.

For a given volume of water, the change in concentration of a given biological state variable C can be expressed as follows:

$$\frac{\partial C}{\partial t} = -\boldsymbol{U} \cdot \nabla C + \nabla \cdot (\kappa \cdot \nabla C) + \text{SMS}(C) \tag{A1}$$

Here, the term $-\boldsymbol{U} \cdot \nabla C$ represents the change in C due to advection, and $\boldsymbol{U} = (u, v, w)$ denotes the velocity of the water in the x, y and z-directions respectively.

For sinking state variables, the speed of vertical sinking ($\boldsymbol{V}_{\text{det}} = (0, 0, w_{\text{det}})$) is added to water's velocity in the advection term.

The turbulent motion is taken into account through the term $\nabla \cdot (\kappa \cdot \nabla C)$ where κ is the diffusivity tensor.

The term $\text{SMS}(C)$, where SMS stands for sources-minus-sinks, represents the changes due to biological processes. This is the term that comprises the main body of biogeochemical models.

Certain state variables are subject to fluxes across the boundaries of the ocean model. For these, the flux between the ocean and the benthos (BenF) is calculated at the bottom of the

26

ocean and the the flux between the ocean and the atmosphere (AtmF) is calculated for the surface layer of the ocean.

In the following, the equations that make up the source-minus-sink code in the biogeochemical model REcoM2 are described.

5 The quota approach makes it necessary to have more tracers than in a model based on fixed ratios, as we need to know the intracellular concentration of each of the modelled elements. REcoM2 has a total of 21 oceanic state variables (Table 4) and four benthos compartments (Table 5).

A1 Sources minus sinks

10 A1.1 DIN and DSi

$$
\mathrm{SMS(DIN)} = \underbrace{\rho_\mathrm{N} \cdot f_T \cdot \mathrm{DON}}_{\text{DON remineralization}} - \underbrace{V_\mathrm{nano}^\mathrm{N} \cdot \mathrm{PhyC_{nano}}}_{\text{N-assimilation, nanophytoplankton}} - \underbrace{V_\mathrm{dia}^\mathrm{N} \cdot \mathrm{PhyC_{dia}}}_{\text{N-assimilation, diatoms}} \tag{A2}
$$

$$
\mathrm{SMS(DSi)} = \underbrace{\rho_\mathrm{Si}^T \cdot \mathrm{DetSi}}_{\text{Remineralization of detritus}} - \underbrace{V^\mathrm{Si} \cdot \mathrm{PhyC_{dia}}}_{\text{Si-assimilation, diatoms}} \tag{A3}
$$

The state variables DON, $\mathrm{PhyC_{nano}}$, $\mathrm{PhyC_{dia}}$ and DetSi are listed in Table 4. The value of the
15 remineralization rate (ρ_N) is listed in Table 6. The temperature dependency of remineralization (f_T) is calculated in Eq. (A54) and the nitrogen and silicon assimilation rates ($V_\mathrm{nano}^\mathrm{N}$, $V_\mathrm{dia}^\mathrm{N}$ and V^Si, Table 4) are calculated in Eq. (A48) and Eq. (A49) respectively. ρ_Si^T will now be explained.
Silicon remineralization: The temperature dependent remineralization rate of silicon (ρ_Si^T, Table 7) is calculated following Kamatani (1982) up until a set maximum value:

$$
20 \quad \rho_\mathrm{Si}^T = \min\left(1.32 \cdot 10^{16}\,\mathrm{day}^{-1} \cdot \exp\left(\frac{-11\,200\,\mathrm{K}}{T}\right), \rho_\mathrm{Si} \cdot f_T\right) \tag{A4}
$$

T is the local temperature. The remineralization rate (ρ_Si) is listed in Table 6 and the temperature dependency (f_T) is calculated in Eq. (A54).

Input from benthos: The bottom grid point of the water further receives remineralized inorganic matter from the benthos:

$$\text{BenF}_{\text{DIN}} = \rho_N^{\text{ben}} \cdot \text{BenthosN} \tag{A5}$$

$$\text{BenF}_{\text{DSi}} = \rho_{\text{Si}}^{\text{ben}} \cdot \text{BenthosSi} \tag{A6}$$

BenF_{DIN} and BenF_{DSi} (Table 8) denote the fluxes of DIN and DSi into the bottom layer of the ocean. ρ_N^{ben} and $\rho_{\text{Si}}^{\text{ben}}$ (Table 6) are constant remineralization rates. BenthosN and BenthosSi denote the vertically integrated benthos concentration of dissolved nitrogen and silicate respectively (Table 5).

A1.2 DFe

The intracellular iron concentration is connected to the intracellular carbon concentration through an assumed constant ratio ($q^{\text{Fe}:\text{C}}$, Table 9). Biological uptake and release of iron is likewise connected to uptake and release of carbon.

$$
\begin{aligned}
\text{SMS}(\text{DFe}) = &- q^{\text{Fe}:\text{C}} \cdot \underbrace{(P_{\text{nano}} - r_{\text{nano}}) \cdot \text{PhyC}_{\text{nano}}}_{\text{Nanophytoplankton net growth}} - q^{\text{Fe}:\text{C}} \cdot \underbrace{(P_{\text{dia}} - r_{\text{dia}}) \cdot \text{PhyC}_{\text{dia}}}_{\text{Diatom net growth}} \\
&+ q^{\text{Fe}:\text{C}} \cdot \underbrace{\epsilon_C^{\text{phy}} \cdot f_{\text{lim, nano}}^{\text{N}:\text{Cmax}} \cdot \text{PhyC}_{\text{nano}}}_{\text{Excretion from nanophytoplankton}} + q^{\text{Fe}:\text{C}} \cdot \underbrace{\epsilon_C^{\text{phy}} \cdot f_{\text{lim, dia}}^{\text{N}:\text{Cmax}} \cdot \text{PhyC}_{\text{dia}}}_{\text{Excretion from diatoms}} \\
&+ q^{\text{Fe}:\text{C}} \cdot \underbrace{\rho_{\text{DetC}} \cdot f_T \cdot \text{DetC}}_{\text{Remineralization of detritus}} + q^{\text{Fe}:\text{C}} \cdot (\underbrace{\epsilon_C^{\text{zoo}} \cdot \text{ZooC}}_{\text{Zooplankton excretion}} + \underbrace{r_{\text{zoo}} \cdot \text{ZooC}}_{\text{and respiration}}) \\
&- \underbrace{\kappa_{\text{Fe}} \cdot \text{DetC} \cdot \text{Fe}'}_{\text{Scavenging}}
\end{aligned} \tag{A7}
$$

The state variables $\text{PhyC}_{\text{nano}}$, PhyC_{dia}, DetC and ZooC are listed in Table 4. The value for the constant Fe : C ratio ($q^{\text{Fe}:\text{C}}$) is listed in Table 9 and the DOC excretion rates from phyto- and zooplankton (ϵ_C^{phy} and ϵ_C^{zoo}) and the degradation rate for detritus C (ρ_{DetC}) are listed in Table 6.

The phytoplankton respiration (r_{nano} and r_{dia}) is calculated in Eq. (A45), the photosynthesis (P_{nano} and P_{dia}) in Eq. (A44), the limitation by intracellular nitrogen ($f_{\text{lim}}^{\text{N:Cmax}}$) is described in Sect. A6.1, and the temperature dependency (f_T) is calculated in Eq. (A54). The respiration by zooplankton (r_{zoo}) is calculated in Eq. (A46) and the scavenging will now be explained.

5 *Scavenging:* The calculation of the scavenging in REcoM2 is based on Parekh et al. (2004), case III. Here, the total concentration of dissolved iron (Fe_{T}) is divided into iron bound to ligands (Fe_L) and free iron (Fe', Table 7):

$$\text{Fe}_{\text{T}} = \text{Fe}_L + \text{Fe}' \tag{A8}$$

10 Iron complexed with organic ligands is protected from scavenging. The total ligand concentration (L_{T}) can be written:

$$L_{\text{T}} = \text{Fe}_L + L' \tag{A9}$$

Here L' denotes the free ligands.

15 We assume that the reaction between free iron and free ligand ($L' + \text{Fe}' \rightleftharpoons \text{Fe}_L$) is fast enough to be in equilibrium:

$$K_{\text{Fe}_L} = \frac{[\text{Fe}_L]}{[\text{Fe}'] \cdot [L']} \tag{A10}$$

By prescribing the value of the conditional stability constant (K_{Fe_L}) as well as the assumed
20 constant total ligand concentration (L_{T}) and combining Eq. (A8), (A9) and (A10), we can calculate the concentration of free iron (Fe'). This is then used to calculate the scavenging of Fe', which is assumed to be correlated with the concentration of detritus carbon (Eq. A7). The values for K_{Fe_L} and L_{T} are listed in Table 9.

The value for the scavenging rate (κ_{Fe}, Table 9) is an important controller of deep water iron
25 concentrations.

Iron input from dust: The surface layer of the ocean receives an input of iron from aeolian dust deposition. Dust is assumed to contain 3.5 % iron of which 1.5 % is instantaneously dissolved in the ocean. Sea ice blocks dust, and the dust falling here is lost from the system.

Iron input from the benthos: The release of iron to the bottom layer of water is assumed to be proportional to the release of inorganic carbon. This parameterization is based on the work by Elrod et al. (2004). It is calculated as follows:

$$\text{BenF}_{\text{Fe}} = \rho_C^{\text{ben}} \cdot \text{BenthosC} \cdot q_{\text{sed}}^{\text{Fe:C}} \tag{A11}$$

Here BenF_{Fe} (Table 8) is the flux of iron into the bottom layer of the ocean. ρ_C^{ben} (Table 6) is the remineralization rate for the benthos carbon and $q_{\text{sed}}^{\text{Fe:C}}$ (Table 9) is the iron:carbon ratio for the flux. BenthosC (Table 5) denotes the vertically integrated carbon concentration in the benthos compartment.

A1.3 DIC

$$\text{SMS(DIC)} = \underbrace{(r_{\text{nano}} - P_{\text{nano}}) \cdot \text{PhyC}_{\text{nano}}}_{\text{Nanophytoplankton net respiration}} + \underbrace{(r_{\text{dia}} - P_{\text{dia}}) \cdot \text{PhyC}_{\text{dia}}}_{\text{Diatom net respiration}} + \underbrace{\rho_C \cdot f_T \cdot \text{DOC}}_{\text{Remineralization of DOC}}$$
$$+ \underbrace{r_{\text{zoo}} \cdot \text{ZooC}}_{\text{Zoo respiration}} + \underbrace{\text{Diss}_{\text{calc}} \cdot \text{DetCalc}}_{\text{Calcite dissolution from detritus}} - \underbrace{\psi \cdot P_{\text{nano}} \cdot \text{PhyC}_{\text{nano}}}_{\text{Calcification}} \tag{A12}$$

The state variables $\text{PhyC}_{\text{nano}}$, PhyC_{dia}, DOC, ZooC and DetCalc are described in Table 4. Respiration by nanophytoplankton (r_{nano}), diatoms (r_{dia}) and zooplankton (r_{zoo}) is calculated in Eq. (A45) and (A46) respectively, and the photosynthesis terms (P_{nano} and P_{dia}) in Eq. (A44).

The value of the remineralization rate ρ_C is listed in Table 6 and the temperature dependency (f_T) is calculated in Eq. (A54).

The dissolution of calcite from detritus ($\text{Diss}_{\text{calc}}$) is calculated in Eq. (A34), and the value of the calcite production ratio (ψ) is listed in Table 10. ψ denotes the percentage of the nanophytoplankton that are calcifiers, and their PIC:POC ratio.

Atmospheric input: The DIC concentration of the surface grid point is affected by the air–sea flux of CO_2. It is calculated according to the guidelines provided by the Ocean Carbon Model Intercomparison Project (Orr et al., 1999). In the calculations the surface water CO_2 concentration, alkalinity, temperature and salinity is taken into account.

Input from benthos: The bottom grid point of the water further receives remineralized inorganic carbon from the benthos:

$$\text{BenF}_{\text{DIC}} = \rho_{\text{C}}^{\text{ben}} \cdot \text{BenthosC} + \text{Diss}_{\text{calc}} \cdot \text{BenthosCalc} \tag{A13}$$

BenF$_{\text{DIC}}$ (Table 8) denotes the flux of DIC into the bottom layer of the ocean and $\rho_{\text{C}}^{\text{ben}}$ (Table 6) is a constant remineralization rate. The calcite dissolution rate (Diss$_{\text{calc}}$) is calculated in Eq. (A34). BenthosC and BenthosCalc (Table 5) denotes the vertically integrated carbon and calcium carbonate concentration in the benthos compartment.

A1.4 Total alkalinity

The model's total alkalinity is changed by phytoplankton uptake of nutrients (nitrate and phosphate), precipitation and dissolution of calcium carbonate and remineralization of organic matter (Wolf-Gladrow et al., 2007). Phosporous is not described in the model, but is taken into account using the constant P : N ratio of 1 : 16.

$$\text{SMS(Alk)} = (1 + 1/16) \cdot \underbrace{V_{\text{nano}}^{\text{N}} \cdot \text{PhyC}_{\text{nano}}}_{\text{N-assimilation, nanophytoplankton}} + (1 + 1/16) \cdot \underbrace{V_{\text{dia}}^{\text{N}} \cdot \text{PhyC}_{\text{dia}}}_{\text{N-assimilation, diatoms}} \tag{A14}$$

$$- (1 + 1/16) \cdot \underbrace{\rho_{\text{N}} \cdot f_T \cdot \text{DON}}_{\text{Remineralization of DON}} + 2 \cdot \underbrace{\text{Diss}_{\text{calc}} \cdot \text{DetCaCO}_3}_{\text{Calcite dissolution from detritus}}$$

$$- 2 \cdot \underbrace{\psi \cdot P_{\text{nano}} \cdot \text{PhyC}_{\text{nano}}}_{\text{Calcification}}$$

The state variables PhyC$_{\text{nano}}$, PhyC$_{\text{dia}}$, DON and DetCalc are described in Table 4. The N-assimilation ($V_{\text{nano}}^{\text{N}}$ and $V_{\text{dia}}^{\text{N}}$) is calculated in Eq. (A48). The remineralization rate (ρ_{N}) can be found in Table 6 and the temperature dependency (f_T) is calculated in Eq. (A54).

Dissolution of calcium carbonate from detritus adds CO_3^{2-} to the water and thereby increases the alkalinity with two moles for each dissolved mole calcium carbonate. Diss$_{\text{calc}}$ is calculated in Eq. (A34).

31

The parameter ψ, specifying the calcifying fraction of the nanophytoplankton, is listed in Table 10 and the photosynthesis (P_{nano}) is calculated in Eq. (A44).

Input from benthos: The alkalinity of the bottom grid point of the water is affected by the remineralization of DIN, and thereby also DIP as well as dissolution of calcite from the benthos:

$$\begin{aligned} \text{BenF}_{\text{Alk}} = (1 + 1/16) \cdot \rho_{\text{N}}^{\text{ben}} \cdot \text{BenthosN} \\ + 2 \cdot \text{Diss}_{\text{calc}} \cdot \text{BenthosCalc} \end{aligned} \tag{A15}$$

BenF_{Alk} (Table 8) denotes the flux of alkalinity into the bottom layer of the ocean. The dissolution rate ($\text{Diss}_{\text{calc}}$) is calculated in Eq. (A34), and the remineralization rate ρ_N^{ben} is listed in Table 6. BenthosN and BenthosC (Table 5) denotes the vertically integrated nitrogen and carbon concentration in the benthos compartment.

A1.5 Phytoplankton N

$$\text{SMS}(\text{PhyN}_{\text{nano}}) = \underbrace{V_{\text{nano}}^{\text{N}} \cdot \text{PhyC}_{\text{nano}}}_{\text{N-assimilation}} - \underbrace{\epsilon_{\text{N}}^{\text{phy}} \cdot f_{\text{lim, nano}}^{\text{N : Cmax}} \cdot \text{PhyN}_{\text{nano}}}_{\text{DON excretion}} - \underbrace{\text{Agg} \cdot \text{PhyN}_{\text{nano}}}_{\text{Aggregation loss}} - \underbrace{G_{\text{nano}}}_{\text{Grazing loss}} \tag{A16}$$

$$\text{SMS}(\text{PhyN}_{\text{dia}}) = \underbrace{V_{\text{dia}}^{\text{N}} \cdot \text{PhyC}_{\text{dia}}}_{\text{N-assimilation}} - \underbrace{\epsilon_{\text{N}}^{\text{phy}} \cdot f_{\text{lim, dia}}^{\text{N : Cmax}} \cdot \text{PhyN}_{\text{dia}}}_{\text{DON excretion}} - \underbrace{\text{Agg} \cdot \text{PhyN}_{\text{dia}}}_{\text{Aggregation loss}} - \underbrace{G_{\text{dia}}}_{\text{Grazing loss}} \tag{A17}$$

The state variables PhyC$_{\text{nano}}$, PhyN$_{\text{nano}}$, PhyC$_{\text{dia}}$ and PhyN$_{\text{dia}}$ are described in Table 4.

The nitrogen assimilation ($V_{\text{nano}}^{\text{N}}$ and $V_{\text{dia}}^{\text{N}}$) is calculated in Eq. (A48) and the constant excretion rate ($\epsilon_{\text{N}}^{\text{phy}}$) is listed in Table 6. When the N : C ratio becomes too high, excretion of DOC is downregulated by the limiter function ($f_{\text{lim}}^{\text{N : Cmax}}$) described in Sect. A6.1. A further loss term is phytoplankton aggregation (Agg), which transfers N to the detritus pools (Eq. A27).

The grazing loss (G_{nano} and G_{dia}) is calculated in Eqs. (A52) and (A53).

A1.6 Phytoplankton C

$$
\begin{aligned}
\text{SMS}(\text{PhyC}_{\text{nano}}) = &\underbrace{(P_{\text{nano}} - r_{\text{nano}}) \cdot \text{PhyC}_{\text{nano}}}_{\text{Net photosynthesis}} - \underbrace{\text{Agg} \cdot \text{PhyC}_{\text{nano}}}_{\text{Aggregation loss}} \\
&- \underbrace{\epsilon_{\text{C}}^{\text{phy}} \cdot f_{\text{lim, nano}}^{\text{N : Cmax}} \cdot \text{PhyC}_{\text{nano}}}_{\text{Excretion of DOC}} - \underbrace{q_{\text{nano}}^{\text{C : N}} \cdot G_{\text{nano}}}_{\text{Grazing loss}}
\end{aligned}
\tag{A18}
$$

$$
\begin{aligned}
\text{SMS}(\text{PhyC}_{\text{dia}}) = &\underbrace{(P_{\text{dia}} - r_{\text{dia}}) \cdot \text{PhyC}_{\text{dia}}}_{\text{Net photosynthesis}} - \underbrace{\text{Agg} \cdot \text{PhyC}_{\text{dia}}}_{\text{Aggregation loss}} \\
&- \underbrace{\epsilon_{\text{C}}^{\text{phy}} \cdot f_{\text{lim, dia}}^{\text{N : Cmax}} \cdot \text{PhyC}_{\text{dia}}}_{\text{Excretion of DOC}} - \underbrace{q_{\text{dia}}^{\text{C : N}} \cdot G_{\text{dia}}}_{\text{Grazing loss}}
\end{aligned}
\tag{A19}
$$

The state variables $\text{PhyC}_{\text{nano}}$ and PhyC_{dia} are described in Table 4. The photosynthesis (P_{nano} and P_{dia}) is calculated in Eq. (A44) and the respiration (r_{nano} and r_{dia}) in Eq. (A45). The constant DOC excretion rate ($\epsilon_{\text{C}}^{\text{phy}}$, Table 6) is downregulated by the limitation factor $f_{\text{lim}}^{\text{N : Cmax}}$ (Sect. A6.1) when the N : C ratio becomes too high.

Aggregation of phytoplankton (Agg) is calculated in Eq. (A27) and grazing (G_{nano} and G_{dia}) in Eqs. (A52) and (A53). $q^{\text{C : N}} = \text{PhyC}/\text{PhyN}$, is used to convert the grazing units from mmol N to mmol C.

A1.7 Phytoplankton CaCO₃

Calcifiers are assumed to comprise a certain fraction of the total nanophytoplankton concentration, specified by the parameter ψ (Table 10), tying the calcite production of calcifiers to the growth of nanophytoplankton.

$$\text{SMS(PhyCalc)} = \underbrace{\psi \cdot P_{\text{nano}} \cdot \text{PhyC}_{\text{nano}}}_{\text{Calcification}} - \underbrace{r_{\text{nano}} \cdot \text{PhyCalc}}_{\text{Respiration}} - \underbrace{G_{\text{nano}} \cdot q_{\text{nano}}^{\text{CaCO}_3:\text{N}}}_{\text{Grazing loss}}$$
$$- \underbrace{\epsilon_{\text{C}}^{\text{phy}} \cdot f_{\text{lim, nano}}^{\text{N}:\text{Cmax}} \cdot \text{PhyCalc}}_{\text{Excretion loss}} - \underbrace{\text{Agg} \cdot \text{PhyCalc}}_{\text{Aggregation loss}} \tag{A20}$$

The state variables $\text{PhyC}_{\text{nano}}$ and PhyCalc are described in Table 4. The values for the calcifier fraction (ψ) is listed in Table 10 and the excretion parameter ($\epsilon_{\text{C}}^{\text{phy}}$) in Table 6. The excretion loss is downregulated by the limiter function $f_{\text{lim, nano}}^{\text{N}:\text{Cmax}}$ (Sect. A6.1) when the intracellular N : C ratio approaches a maximum value. The photosynthesis (P_{nano}) is calculated in Eq. (A44), the respiration (r_{nano}) in Eq. (A45), the grazing on nanophytoplankton (G_{nano}) in Eq. (A52) and the aggregation rate (Agg) is calculated in Eq. (A27). $q_{\text{nano}}^{\text{CaCO}_3:\text{N}} = \text{PhyCaCO}_3/\text{PhyN}_{\text{nano}}$.

A1.8 Diatom silicon

$$\text{SMS(PhySi)} = \underbrace{V^{\text{Si}} \cdot \text{PhyC}_{\text{dia}}}_{\text{Diatom Si-assimilation}} - \underbrace{\epsilon_{\text{N}}^{\text{phy}} \cdot f_{\text{lim, dia}}^{\text{N}:\text{Cmax}} \cdot \text{PhySi}}_{\text{Excretion to detritus}} - \underbrace{\text{Agg} \cdot \text{PhySi}}_{\text{Aggregation loss}} - \underbrace{G_{\text{dia}} \cdot q^{\text{Si}:\text{N}}}_{\text{Grazing loss}} \tag{A21}$$

The state variables PhyC_{dia} and PhySi are described in Table 4. The silicon assimilation rate (V^{Si}) is calculated in Eq. (A49), the aggregation rate (Agg) in Eq. (A27) and the grazing on diatoms (G_{dia}) is calculated in Eq. (A53). The limiter function ($f_{\text{lim}}^{\text{N}:\text{Cmax}}$) is described in Sect. A6.1. The value of the excretion parameter ($\epsilon_{\text{N}}^{\text{phy}}$) is listed in Table 6 and the intracellular ratio between diatom silicon and carbon is defined as $q^{\text{Si}:\text{N}} = \text{PhySi}/\text{PhyN}_{\text{dia}}$.

A1.9 Phytoplankton Chl a

$$\text{SMS}(\text{PhyChl}_{\text{nano}}) = \underbrace{S_{\text{nano}}^{\text{chl}} \cdot \text{PhyC}_{\text{nano}}}_{\text{Chl } a \text{ synthesis}} - \underbrace{G_{\text{nano}} \cdot q_{\text{nano}}^{\text{Chl}:\text{N}}}_{\text{Grazing loss}} - \underbrace{\text{deg}_{\text{chl}} \cdot \text{PhyChl}_{\text{nano}}}_{\text{Degradation loss}} - \underbrace{\text{Agg} \cdot \text{PhyChl}_{\text{nano}}}_{\text{Aggregation loss}}$$
(A22)

$$\text{SMS}(\text{PhyChl}_{\text{dia}}) = \underbrace{S_{\text{dia}}^{\text{chl}} \cdot \text{PhyC}_{\text{dia}}}_{\text{Chl } a \text{ synthesis}} - \underbrace{G_{\text{dia}} \cdot q_{\text{dia}}^{\text{Chl}:\text{N}}}_{\text{Grazing loss}} - \underbrace{\text{deg}_{\text{chl}} \cdot \text{PhyChl}_{\text{dia}}}_{\text{Degradation loss}} - \underbrace{\text{Agg} \cdot \text{PhyChl}_{\text{dia}}}_{\text{Aggregation loss}}$$
(A23)

The state variables $\text{PhyC}_{\text{nano}}$, PhyC_{dia}, $\text{PhyChl}_{\text{nano}}$ and $\text{PhyChl}_{\text{dia}}$ are described in Table 4. The chlorophyll a synthesis (S^{chl}) is calculated in Eq. (A47), the aggregation (Agg) in Eq. (A27) and the degradation parameter (deg_{chl}) is listed in Table 6. The grazing fluxes (G_{nano} and G_{dia}) are calculated in Eqs. (A52) and (A53). The conversion factor from mmol N to mg Chl a is defined as $q^{\text{Chl}:\text{N}} = \text{PhyChl}/\text{PhyN}$.

A1.10 Zooplankton

$$\text{SMS}(\text{ZooN}) = \underbrace{\gamma \cdot (G_{\text{nano}} + G_{\text{dia}})}_{\text{Grazing on phytoplankton}} - \underbrace{m_{\text{zoo}} \cdot \text{ZooN}^2}_{\text{Zooplankton mortality}} - \underbrace{\epsilon_{\text{N}}^{\text{zoo}} \cdot \text{ZooN}}_{\text{Excretion of DON}}$$
(A24)

$$\text{SMS}(\text{ZooC}) = \underbrace{\gamma \cdot (G_{\text{nano}} \cdot q_{\text{nano}}^{\text{C}:\text{N}} + G_{\text{dia}} \cdot q_{\text{dia}}^{\text{C}:\text{N}})}_{\text{Grazing on phytoplankton}} - \underbrace{m_{\text{zoo}} \cdot \text{ZooN}^2 \cdot q_{\text{zoo}}^{\text{C}:\text{N}}}_{\text{Zooplankton mortality}} - \underbrace{r_{\text{zoo}} \cdot \text{ZooC}}_{\text{Respiration loss}}$$
$$- \underbrace{\epsilon_{\text{C}}^{\text{zoo}} \cdot \text{ZooC}}_{\text{Excretion of DOC}}$$
(A25)

The state variables ZooN and ZooC are described in Table 4. It is assumed, due to sloppy feeding, that only a fraction of the grazed phytoplankton (γ, Table 10) enters the zooplankton pool. The rest is transferred to detritus.

Grazing by nanophytoplankton and diatoms (G_{nano} and G_{dia}) is calculated in Eqs. (A52) and (A53). The respiration by zooplankton (r_{zoo}) is calculated in Eq. (A46). The value of the

mortality paramter (m_{zoo}) is listed in Table 10 and the DON and DOC excretion (ϵ_N^{zoo} and ϵ_C^{zoo}) in Table 6.

The quotas $q_{nano}^{C:N}$ and $q_{dia}^{C:N}$ convert the units of the grazing from mmol N to mmol C and are defined as follows: $q_{nano}^{C:N} = PhyC_{nano}/PhyN_{nano}$ and $q_{dia}^{C:N} = PhyC_{dia}/PhyN_{dia}$.

A1.11 Detritus N and C

$$
\begin{aligned}
\text{SMS(DetN)} &= \underbrace{(G_{nano} + G_{dia}) \cdot (1 - \gamma)}_{\text{Sloppy feeding}} + \underbrace{m_{zoo} \cdot \text{ZooN}^2}_{\text{Zooplankton mortality}} \\
&+ \underbrace{\text{Agg} \cdot (\text{PhyN}_{nano} + \text{PhyN}_{dia})}_{\text{Phytoplankton aggregation}} - \underbrace{\rho_{DetN} \cdot f_T \cdot \text{DetN}}_{\text{Degradation to DON}} \\
\text{SMS(DetC)} &= \underbrace{(G_{nano} \cdot q_{nano}^{C:N} + G_{dia} \cdot q_{dia}^{C:N}) \cdot (1 - \gamma)}_{\text{Sloppy feeding}} + \underbrace{m_{zoo} \cdot \text{ZooN}^2 \cdot q_{zoo}^{C:N}}_{\text{Zooplankton mortality}} \\
&+ \underbrace{\text{Agg} \cdot (\text{PhyC}_{nano} + \text{PhyC}_{dia})}_{\text{Phytoplankton aggregation}} - \underbrace{\rho_{DetC} \cdot f_T \cdot \text{DetC}}_{\text{Degradation to DOC}}
\end{aligned}
\tag{A26}
$$

The state variables ZooN, PhyN$_{nano}$, PhyN$_{dia}$, DetN and DetC are described in Table 4. Due to sloppy feeding, the grazed phytoplankton partly goes to the zooplankton pool and partly to the detritus pool, depending on the grazing efficiency γ (Table 10). The grazing (G_{nano} and G_{dia}) is calculated in Eqs. (A52) and (A53).

The quadratic mortality loss from zooplankton (m_{zoo}) is listed in Table 10. The temperature dependent degradation of detritus to DOM (ρ_{DetN} and ρ_{DetC}) in Table 6, and the temperature dependency (f_T) is calculated in Eq. (A54).

The quotas $q_{nano}^{C:N} = PhyC_{nano}/PhyN_{nano}$, $q_{dia}^{C:N} = PhyC_{dia}/PhyN_{dia}$ and $q_{zoo}^{C:N} = ZooC/ZooN$ are used to convert the units from mmol N to mmol C.

Aggregation: The aggregation rate (Agg, Table 7) is proportional to the concentration of nanophytoplankton, diatoms and detritus:

$$
\text{Agg} = \phi_{phy} \cdot (\text{PhyN}_{nano} + \text{PhyN}_{dia}) + \phi_{det} \cdot \text{DetN}
\tag{A27}
$$

The values of the maximum aggregation loss parameters (ϕ_{phy} and ϕ_{det}) are listed in Table 10. The state variables PhyN$_{\text{nano}}$, PhyN$_{\text{dia}}$ and DetN are described in Table 4.

Sinking: In the model the detritus is subject to sinking, which increases linearly with depth. The sinking speed (w_{det}, Table 7) is based on the work by Kriest and Oschlies (2008).

$$w_{\text{det}} = 0.0288\,\text{day}^{-1} \cdot z + w_0 \tag{A28}$$

Here z denotes the current depth and w_0 is the sinking speed at the surface (Table 10).

Loss to benthos: When the sinking detritus reaches the bottom grid point it is assumed that it continues sinking into the benthic compartment with the speed w_{det} (Eq. A28). This leads to a detrital flux (BenF$_{\text{DetN}}$ and BenF$_{\text{DetC}}$, Table 8) from the water column to the benthos:

$$\text{BenF}_{\text{DetN}} = -w_{\text{det}} \cdot \text{DetN} \tag{A29}$$
$$\text{BenF}_{\text{DetC}} = -w_{\text{det}} \cdot \text{DetC} \tag{A30}$$

The state variables DetN and DetC are described in Table 4.

A1.12 Detritus Si

$$\text{SMS}(\text{DetSi}) = (\underbrace{\epsilon_N^{\text{phy}} \cdot f_{\text{lim, dia}}^{\text{N : Cmax}} + \underbrace{\text{Agg}}_{\text{Aggregation}}) \cdot \text{PhySi}}_{\text{Diatom excretion}} + \underbrace{G_{\text{dia}} \cdot q^{\text{Si : N}}}_{\text{Sloppy feeding}} - \underbrace{\rho_{\text{Si}}^{T} \cdot f_T \cdot \text{DetSi}}_{\text{Remineralization to DSi}} \tag{A31}$$

The state variables PhySi and DetSi are described in Table 4. The limiter function ($f_{\text{lim}}^{\text{N : Cmax}}$) is described in Sect. A6.1. The aggregation rate (Agg) is calculated in Eq. (A27), the grazing on diatoms (G_{dia}) in Eq. (A53), the remineralization rate (ρ_{Si}^{T}) in Eq. (A4) and the temperature dependency of remineralization (f_T) is calculated in Eq. (A54). The value of the excretion parameter (ϵ_N^{phy}) is listed in Table 6. The intracellular ratio between diatom silicon and carbon is defined as $q^{\text{Si : N}} = \text{PhySi}/\text{PhyN}_{\text{dia}}$.

Loss to benthos: When the sinking detritus reaches the bottom grid point it is assumed that it continues sinking into the benthic compartment with the speed w_{det} (Eq. A28). This leads to a detrital flux (BenF$_{DetSi}$, Table 8) from the water column to the benthos:

$$\text{BenF}_{\text{DetSi}} = -w_{\text{det}} \cdot \text{DetSi} \tag{A32}$$

The state variable DetSi is described in Table 4.

A1.13 Detritus CaCO₃

$$\text{SMS}(\text{DetCalc}) = \underbrace{\epsilon_C^{\text{phy}} \cdot f_{\text{lim, nano}}^{\text{N : Cmax}} \cdot \text{PhyCalc}}_{\text{Nanophytoplankton excretion}} + (\underbrace{\text{Agg}}_{\text{Aggregation}} + \underbrace{r_{\text{nano}}}_{\text{Respiration}}) \cdot \text{PhyCalc} \tag{A33}$$
$$+ \underbrace{G_{\text{nano}} \cdot q_{\text{nano}}^{\text{CaCO}_3 : \text{N}}}_{\text{Grazing loss}} - \underbrace{\text{Diss}_{\text{calc}} \cdot \text{DetCalc}}_{\text{Dissolution to DIC}}$$

The state variables PhyCalc and DetCalc are described in Table 4. The limiter function ($f_{\text{lim}}^{\text{N : Cmax}}$) is described in Sect. A6.1. The aggregation rate (Agg) is calculated in Eq. (A27), the respiration rate (r_{nano}) in Eq. (A45) and the nanophytoplankton grazing rate (G_{nano}) in Eq. (A52). The excretion rate (ϵ_C^{phy}) is listed in Table 6, the ratio $q_{\text{nano}}^{\text{CaCO}_3 : \text{N}} = \text{PhyCalc}/\text{PhyN}_{\text{nano}}$ and the calcite dissolution rate will now be explained.

Calcite dissolution: As the detritus calcite sinks through the water column it is subject to dissolution (Diss$_{calc}$, Table 7) occurring on a length scale of $3500\,\text{m}$ (Yamanaka and Tajika, 1996).

$$\text{Diss}_{\text{calc}} = \frac{w_z}{3500\,\text{m}} \tag{A34}$$

w_z denotes the sinking speed at depth z and is calculated in Eq. (A28).

Loss to benthos: When the sinking detritus reaches the bottom grid point it is assumed that it continues sinking into the benthic compartment with the speed w_{det} (Eq. A28). This leads to

a detrital flux ($\text{BenF}_{\text{DetCalc}}$, Table 8) from the water column to the benthos:

$$\text{BenF}_{\text{DetCalc}} = -w_{\text{det}} \cdot \text{DetCaCO}_3 \tag{A35}$$

The state variable DetCalc is described in Table 4.

A1.14 Dissolved organic material

$$\text{SMS(DON)} = \underbrace{\epsilon_N^{\text{phy}} \cdot f_{\text{lim, nano}}^{\text{N : Cmax}} \cdot \text{PhyN}_{\text{nano}}}_{\text{Nanophytoplankton excretion}} + \underbrace{\epsilon_N^{\text{phy}} \cdot f_{\text{lim, dia}}^{\text{N : Cmax}} \cdot \text{PhyN}_{\text{dia}}}_{\text{Diatom excretion}} \tag{A36}$$

$$+ \quad \underbrace{\epsilon_N^{\text{zoo}} \cdot \text{ZooN}}_{\text{Zooplankton excretion}} + \underbrace{\rho_{\text{DetN}} \cdot f_T \cdot \text{DetN}}_{\text{Detritus degradation}} - \underbrace{\rho_N \cdot f_T \cdot \text{DON}}_{\text{Remineralization}}$$

$$\text{SMS(DOC)} = \underbrace{\epsilon_C^{\text{phy}} \cdot f_{\text{lim, nano}}^{\text{N : Cmax}} \cdot \text{PhyC}_{\text{nano}}}_{\text{Nanophytoplankton excretion}} + \underbrace{\epsilon_C^{\text{phy}} \cdot f_{\text{lim, dia}}^{\text{N : Cmax}} \cdot \text{PhyC}_{\text{dia}}}_{\text{Diatom excretion}} \tag{A37}$$

$$+ \quad \underbrace{\epsilon_C^{\text{zoo}} \cdot \text{ZooC}}_{\text{Zooplankton excretion}} + \underbrace{\rho_{\text{DetC}} \cdot f_T \cdot \text{DetC}}_{\text{Detritus degradation}} - \underbrace{\rho_C \cdot f_T \cdot \text{DOC}}_{\text{Remineralization}}$$

The state variables are described in Table 4. The values for excretion of nitrogen and carbon from phyto- and zooplankton (ϵ_N^{phy}, ϵ_C^{phy}, ϵ_N^{zoo} and ϵ_C^{zoo}) are listed in Table 6 along with the degradation rates for detritus (ρ_{detN} and ρ_{detC}) and remineralization rates of DON and DOC (ρ_N and ρ_C). The limitation factors ($f_{\text{lim, nano}}^{\text{N : Cmax}}$ and $f_{\text{lim, dia}}^{\text{N : Cmax}}$) are described in Sect. A6.1 and the temperature dependency (f_T) is calculated in Eq. (A54).

A2 Sources minus sinks, benthos

The model has a benthos compartment which consists of one layer. Matter is supplied to this layer through sinking detritus, and it hence has pools of nitrogen, silicon, carbon and calcite. When sinking detritus reaches the bottom it continues sinking into the benthos with the speed calculated by Eq. (A28) and is thus lost from the water column. In the benthos, the detritus

is assumed to be remineralized to dissolved inorganic matter. This is then re-released to the water's pools of dissolved inorganic matter (DIN, DIC, Alk and DSi):

$$\text{SMS}(\text{BenthosN}) = w_{\text{det}} \cdot \text{DetN} - \rho_{\text{N}}^{\text{ben}} \cdot \text{BenthosN} \tag{A38}$$

$$\text{SMS}(\text{BenthosSi}) = w_{\text{det}} \cdot \text{DetSi} - \rho_{\text{Si}}^{\text{ben}} \cdot \text{BenthosSi} \tag{A39}$$

$$\text{SMS}(\text{BenthosC}) = w_{\text{det}} \cdot \text{DetC} - \rho_{\text{C}}^{\text{ben}} \cdot \text{BenthosC} \tag{A40}$$

$$\text{SMS}(\text{BenthosCalc}) = w_{\text{det}} \cdot \text{DetCalc} - \text{Diss}_{\text{calc}} \cdot \text{BenthosCalc} \tag{A41}$$

The state variables are described in Table 4 (DetN, DetSi, DetC and DetCalc) and Table 5 (BenthosN, BenthosSi, BenthosC and BenthosCalc). The remineralization rates ($\rho_{\text{N}}^{\text{ben}}$, $\rho_{\text{Si}}^{\text{ben}}$ and $\rho_{\text{C}}^{\text{ben}}$) are listed in Table 6 and the calcite dissolution rate ($\text{Diss}_{\text{calc}}$) is calculated in Eq. (A34).

A3 Phytoplankton growth

A3.1 Photosynthesis

The rate of the C-specific photosynthesis is calculated for both nanophytoplankton and diatoms (P_{nano} and P_{dia}, Table 7).

The calculation is based on the work by Geider et al. (1998) and differs between nanophytoplankton and diatoms in the nutrient limitation; nanophytoplankton is limited by iron and nitrogen while diatoms are additionally limited by silicon.

$$P_{\text{max}}^{\text{nano}} = \mu_{\text{C}}^{\text{max}} \cdot \min\left(f_{\text{lim, nano}}^{\text{Fe}}, f_{\text{lim, nano}}^{\text{N : Cmin}}\right) \cdot f_T \tag{A42}$$

$$P_{\text{max}}^{\text{dia}} = \mu_{\text{C}}^{\text{max}} \cdot \min\left(f_{\text{lim, dia}}^{\text{Fe}}, f_{\text{lim, dia}}^{\text{N : Cmin}}, f_{\text{lim, dia}}^{\text{Si : Cmin}}\right) \cdot f_T \tag{A43}$$

Nutrient limitation is calculated using the "Liebig law of the minimum", in which the most limiting nutrient limits production (O'Neill et al., 1989).

The value of $\mu_{\text{C}}^{\text{max}}$ can be found in Table 11. The limitation terms ($f_{\text{lim}}^{\text{N : Cmin}}$, $f_{\text{lim}}^{\text{Si : Cmin}}$ and $f_{\text{lim}}^{\text{Fe}}$) differ somewhat from the formlation in Geider et al. (1998) and are described in Sect. A6.2 and the temperature dependency (f_T) is calculated in Eq. (A54).

The actual C-specific photosynthesis rate depends on how much photosynthetically available radiation (PAR, Table 7) the cell can harvest. This is controlled by the light harvesting efficiency (α) and the intracellular Chl to C ratio as well as the available light.

$$P = P_{\text{max}} \cdot \left(1.0 - \exp \left(\frac{-\alpha \cdot q^{\text{Chl}:\text{C}} \cdot \text{PAR}}{P_{\text{max}}} \right) \right) \tag{A44}$$

The C-specific photosynthesis rate is calculated for both nanophytoplankton and diatoms; P_{nano} and P_{dia} respectively (Table 7).

The values for the light harvesting efficiencies (α_{nano} and α_{dia}) are listed in Table 11, the apparent maximum photosynthetic rate (P_{max}) is calculated in Eqs. (A42) and (A43) and we define $q^{\text{Chl}:\text{C}} = \text{PhyChl}/\text{PhyC}$.

A3.2 Respiration

Phytoplankton: The phytoplankton respiration rate is calculated for both nanophytoplankton and diatoms respectively (r_{nano} and r_{dia}, Table 7):

$$r = \underbrace{\text{res} \cdot f_{\text{lim}}^{\text{N}:\text{Cmax}}}_{\text{Cost of maintenance}} + \underbrace{\zeta \cdot V^{\text{N}}}_{\text{Cost of N-assim}} \tag{A45}$$

The values for the maintenance respiration rate (res) and the cost of biosynthesis (ζ) can be found in Table 11. The limiter function ($f_{\text{lim}}^{\text{N}:\text{Cmax}}$) is described in Sect. A6.1 and the nitrogen assimilation rate ($V_{\text{nano}}^{\text{N}}$ and $V_{\text{dia}}^{\text{N}}$) is calculated in Eq. (A48).

Zooplankton: When the intracellular C : N ratio in zooplankton exceeds the Redfield ratio, a temperature dependent respiration (r_{zoo}, Table 7) is assumed to drive it back with a time scale τ. Else, the respiration is zero.

$$r_{\text{zoo}} = \max \left(0 \, \text{day}^{-1}, \frac{q_{\text{zoo}}^{\text{C}:\text{N}} - q_{\text{Standard}}^{\text{C}:\text{N}}}{\tau} \cdot f_T \right) \tag{A46}$$

The time scale for respiration (τ) is given in Table 11. The temperature dependence (f_T) is calculated in Eq. (A54), and we define the ratios $q_{\text{zoo}}^{\text{C}:\text{N}} = \text{ZooC}/\text{ZooN}$ and $q_{\text{Standard}}^{\text{C}:\text{N}} = 106\text{C}/16\text{N}$.

41

A3.3 Chlorophyll a synthesis

Chlorophyll a synthesis is coupled to N-uptake in REcoM2. The uptake of nitrogen by the phytoplankton (V^N) is converted to chlorophyll units with a maximum Chl : N ratio ($q_{max}^{Chl:N}$). This highest possible chlorophyll synthesis rate can then be downregulated by the ratio between the actual photosynthesis and the light absorption, leading to a smaller rate when photosynthesis is small.

The chlorophyll a synthesis is calculated for both nanophytoplankton and diatoms (S_{nano}^{Chl} and S_{dia}^{Chl}, Table 7).

$$S^{chl} = V^N \cdot q_{max}^{Chl:N} \cdot \min\left(1, \frac{P}{\alpha \cdot q^{Chl:C} \cdot PAR}\right) \tag{A47}$$

The nitrogen assimilation (V_{nano}^N and V_{dia}^N) is calculated in Eq. (A48), and the value for the maximum Chl : N ratio ($q_{max}^{Chl:N}$) can be seen in Table 11.

The C-specific photosynthesis (P_{nano} and P_{dia}) is calculated in Eq. (A44), and the values for α_{nano} and α_{dia} are listed in Table 11. PAR denotes the photosynthetically available radiation and we define $q^{Chl:C} = PhyChl/PhyC$.

A3.4 Nitrogen and silicon assimilation

Nitrogen: The carbon specific N-assimilation rate is based on the maximum rate of carbon specific photosynthesis (P_{max}), which is then modulated by the maximum N : C uptake ratio ($\sigma_{N:C}$) and by the intracellular quota between N and C ($f_{lim}^{N:Cmax}$), which downregulates N-assimilation when the N : C ratio approaches a maximum value (Sect. A6.1). The concentration of DIN in the surrounding water modifies the N-assimilation through Michaelis–Menten kinetics.

N-assimilation is calculated for both diatoms and nanophytoplankton (V_{nano}^N and V_{dia}^N, Table 7).

$$V^N = V_{cm} \cdot P_{max} \cdot \sigma_{N:C} \cdot f_{lim}^{N:Cmax} \cdot \frac{DIN}{K_N + DIN} \tag{A48}$$

The values of the parameters for V_{cm}, $\sigma_{N:C}$, K_N^{nano} and K_N^{dia} are listed in Table 11. The maximum rates of photosynthesis (P_{max}^{nano} and P_{max}^{dia}) are calculated in Eqs. (A42) and (A43) respectively and $f_{lim}^{N:Cmax}$ is described in Sect. A6.1. DIN denotes the surrounding water's DIN concentration.

5 *Silicon*: Silicon is only taken up by diatoms. The maximum silicon uptake rate is calculated as the maximum photosynthetic rate (μ_C^{max}) multiplied by the maximum Si : C ratio ($\sigma_{Si:C}$) and the scaling factor for the maximum nitrogen uptake. The actual uptake depends on the surrounding water's silicon concentration through Michaelis–Menten kinetics and the temperature dependency (f_T). It is additionally downregulated when the N : C or Si : C ratios become too high

10 ($f_{lim}^{Si:Cmax}$ and $f_{lim\,dia}^{N:Cmax}$). The N : C ratio is taken into account as a too high ratio indicates that the intracellular concentration of energy rich carbon molecules becomes too low to use energy on silicon uptake.

$$V^{Si} = V_{cm} \cdot \mu_C^{max} \cdot f_T \cdot \sigma_{Si:C} \cdot f_{lim}^{SiCmax} \cdot f_{lim\,dia}^{NCmax} \cdot \frac{DSi}{K_{Si} + DSi} \tag{A49}$$

15 The scaling factor for the N-uptake (V_{cm}) and the C-specific photosynthesis rate (μ_C^{max}) are listed in Table 11 along with the maximum Si : C uptake ratio ($\sigma_{Si:C}$). The temperature dependency (f_T) is calculated in Eq. (A54), and the limitation by the intracellular ratios Si : C and N : C ($f_{lim}^{Si:Cmax}$ and $f_{lim,\,dia}^{N:Cmax}$) are described in Sects. A6.3 and A6.1 respectively. K_{Si} is listed in Table 11, and DSi denotes the surrounding water's concentration of DSi.

A4 Grazing

REcoM2 entails a single zooplankton class, which is also the highest trophic level in the model. Grazing on both nanophytoplankton and diatoms is calculated using a Type 3 Sigmoidal model as described by Gentleman et al. (2003).

The maximum grazing rate (G_{max}) is modulated by the temperature through the Arrhenius

25 function (f_T) and by the prey availability through a quadratic Michaelis–Menten function. The model has fixed preferences for both phytoplankton classes and G' (Table 7) is the phytoplank-

ton concentration available for food intake, in our case:

$$G' = \text{PhyN}_{\text{nano}} + \text{PhyN}_{\text{dia}} \cdot f_Z^{\text{dia}} \tag{A50}$$

Here, the parameter f_Z^{dia} (Table 12) specifies the relative grazing preference for diatoms.
5 The total grazing (G_{tot}, Table 7) is calculated as follows:

$$G_{\text{tot}} = G_{\text{max}} \cdot \frac{G'^2}{K_G + G'^2} \cdot f_T \cdot \text{ZooN} \tag{A51}$$

This total grazing can be divided into the grazing on nanophytoplankton and diatoms respectively (G_{nano} and G_{dia}, Table 7):

10 $$G_{\text{nano}} = G_{\text{tot}} \cdot \frac{\text{PhyN}_{\text{nano}}}{G'} \tag{A52}$$

$$G_{\text{dia}} = G_{\text{tot}} \cdot \frac{\text{PhyN}_{\text{dia}} \cdot f_Z^{\text{dia}}}{G'} \tag{A53}$$

The values for the maximum grazing rate (G_{max}), the half saturation constant (K_G) and the fraction of diatoms available for grazing (f_Z^{dia}) are listed in Table 12. The temperature dependency
15 (f_T) is calculated in Eq. (A54) and the state variables are described in Table 4.

A5 Temperature dependence of rates

Temperature dependence of metabolic rates (f_t, Table 7) is taken into account through an Arrhenius function:

20 $$f_T = \exp\left(-4500\text{K} \cdot \left(T^{-1} - T_{\text{ref}}^{-1}\right)\right) \tag{A54}$$

Here, T is the local temperature in Kelvin and T_{ref} is a reference temperature (Table 13). The value $4500\,\text{K}$ is the slope of the linear part of the Arrhenius function. Figure 21 illustrates how the metabolic rates decrease for $T < T_{\text{ref}}$ and increase for $T > T_{\text{ref}}$.

A6 Nutrient limitation

One factor controlling the metabolic processes in the phytoplankton is the intracellular ratios between nutrients and carbon.

Five different limiters are used for this; one that downregulates uptake of N and release of C
when the N : C ratio becomes too high ($f_{\lim}^{N : Cmax}$, Sect. A6.1), three that downregulate photosynthesis when the nutrient : C ratios become too low ($f_{\lim}^{N : Cmin}$, $f_{\lim}^{Si : Cmin}$ and $f_{\lim}^{Fe}$, Sect. A6.2) and one that downregulates silicon assimilation when the Si : C ratio becomes too high ($f_{\lim}^{Si : Cmax}$, Sect. A6.3).

These limiters will now be described after a general explanation of the function.

The way the intracellular ratios between nutrients and carbon limit uptake in the model is based on the work by Geider et al. (1998), but has been modified to the non-linear function, which is calculated as follows:

$$f_{\lim}(\text{slope}, q_1, q_2) = 1 - \exp(-\text{slope}(|\Delta q| - \Delta q)^2) \tag{A55}$$

Here, $\Delta q = q_1 - q_2$ is the difference between the intracellular nutrient:C quota and a prescribed max or min quota, which is chosen depending on the situation.

The dimensionless constant slope regulates the degree of limitation for a given Δq.

A6.1 Intracellular regulation of N-uptake and C-release

Here we take a closer look at the limiter $f_{\lim}^{N : Cmax}$, which downregulates the metabolic processes
listed in Table 14 when the intracellular N : C ratio becomes too high.

It is calculated with Eq. A55 using the following parameters:

$$\text{slope} = \text{slope}_{\max}^{N}, q_1 = q^{N : Cmax}, q_2 = q^{N : C}$$

$\text{slope}_{\max}^{N}$ is listed in Table 13 along with the prescribed maximum N : C quota ($q^{N : Cmax}$). $q^{N : C}$
is the current intracellular quota.

In Fig. 22 it is illustrated how the limiter function changes with changing intracellular N : C quota; when the intracellular concentration of nitrogen increases as compared to carbon, the

45

rate of the processes that are affected by the limiter will be downregulated. Total limitation ($f_{\lim}^{N:Cmax} = 0$) occurs when the quota becomes equal to or higher than 0.2, or the equivalent of 21.2N : 106C.

A6.2 Intracellulare regulation of C-uptake

Photosynthesis is limited by the nutrients iron, nitrogen and in the case of diatoms also silicon.

Nitrogen and silicon limitation: In the case of N and Si, the regulation is controlled by the intracellular ratios N : C ($f_{\lim}^{N:Cmin}$) and Si : C ($f_{\lim}^{Si:Cmin}$). These limiters downregulate the rate of photosynthesis when the intracellular nutrient : C ratios become too low (Fig. 23).

They are calculated with Eq. (A55) using the following parameters (Table 13):

$$\text{slope} = \text{slope}_{min}^{N}, q_1 = q^{N:Cmin}, q_2 = q^{N:C}$$
$$\text{slope} = \text{slope}_{min}^{Si}, q_1 = q^{Si:Cmin}, q_2 = q^{Si:C}$$

Iron: For iron, the water's concentration is used to calculate the limitation. This is done using Michaelis–Menten kinetics:

$$f_{\lim}^{Fe} = \frac{Fe}{K_{Fe} + Fe} \tag{A56}$$

The half saturation constants (K_{Fe}^{nano} and K_{Fe}^{dia}) are listed in Table 13.

A6.3 Intracellular regulation of Si-uptake

Diatom uptake of silicon is downregulated by the function $f_{\lim}^{Si:Cmax}$ (Fig. 24) when the intracellular Si : C ratio exceeds a set limit. The limiter function is described in Eq. (A55) and is calculated using the following variables (Table 13):

$$\text{slope} = \text{slope}_{max}^{Si}, q_1 = q^{Si:C}, q_2 = q^{Si:Cmax}$$

46

plus-0.25ex minus-.2exSupplementary material

The supplements contain the full code for REcoM2 along with a manual for REcoM2-FESOM, containing an overview of the code structure and instructions for running the coupled model.

Supplementary material related to this article is available online at:
http://www.geosci-model-dev-discuss.net/0/1/2014/gmdd-0-1-2014-supplement.zip.

References

Alvain, S., Moulin, C., Dandonneau, Y., and Bréon, F.: Remote sensing of phytoplankton groups in case 1 waters from global SeaWiFS imagery, Deep Sea Research Part I: Oceanographic Research Papers, 52, 1989 – 2004, doi:http://dx.doi.org/10.1016/j.dsr.2005.06.015, http://www.sciencedirect.com/science/article/pii/S0967063705001536, 2005.

Assmann, K., Bentsen, M., Segschneider, J., and Heinze, C.: An isopycnic ocean carbon cycle model, Geosci. Model Dev., 3, 143–167, doi:10.5194/gmd-3-143-2010, 2010.

Aumont, O. and Bopp, L.: Globalizing results from ocean in situ iron fertilization studies, Global Biogeochem. Cy., 20, doi:10.1029/2005GB002591, 2006.

Aumont, O., Orr, J., Monfray, P., Madec, G., and Maier-Reimer, E.: Nutrient trapping in the equatorial Pacific: The ocean circulation solution, Global Biogeochem. Cy., 13, 351–369, doi:10.1029/GBCYEP000013000002000351000001, 1999.

Aumont, O., Maier-Reimer, E., Blain, S., and Monfray, F.: An ecosystem model of the global ocean including Fe, Si, P colimitations, Global Biogeochem. Cy., 17, doi:10.1029/2001GB001745, 2003.

Behrenfeld, M. J.: Abandoning Sverdrup's critical depth hypothesis on phytoplankton blooms, Ecology, 91, 977–989, doi:10.3410/f.2137018.1737130, 2010.

Behrenfeld, M. J. and Falkowski, P. G.: Photosynthetic rates derived from satellite-based chlorophyll concentration, Limnol. Oceanogr., 42, 1–20, doi:10.4319/lo.1997.42.1.0001, 1997.

Behrenfeld, M. J., O'Malley, R. T., Siegel, D. A., McClain, C. R., Sarmiento, J. L., Feldman, G. C., Milligan, A. J., Falkowski, P. G., Letelier, R. M., and Boss, E. S.: Climate-driven trends in contemporary ocean productivity, Nature, 444, 752–755, doi:10.1038/nature05317, 2006.

Bernard, C., Dürr, H., Heinze, C., Segschneider, J., and Maier-Reimer, E.: Contribution of riverine nutrients to the silicon biogeochemistry of the global ocean–a model study, Biogeosciences, 8, 551–564, doi:10.5194/bg-8-551-2011, 2011.

Bopp, L., Resplandy, L., Orr, J. C., Doney, S. C., Dunne, J. P., Gehlen, M., Halloran, P., Heinze, C., Ilyina, T., Séférian, R., Tjiputra, J., and Vichi, M.: Multiple stressors of ocean ecosystems in the 21st century: projections with CMIP5 models, Biogeosciences, 10, 6225–6245, doi:10.5194/bg-10-6225-2013, http://www.biogeosciences.net/10/6225/2013/, 2013.

Broecker, W. S., Peng, T.-H., and Beng, Z.: Tracers in the Sea, Lamont-Doherty Geological Observatory, Columbia University, Palisades, New York, 1982.

Carr, M.-E., Friedrichs, M. A. M., Schmeltz, M., Noguchi Aita, M., Antoine, D., Arrigo, K. R., Asanuma, I., Aumont, O., Barber, R., Behrenfeld, M., Bidigare, R., Buitenhuis, E. T., Campbell, J., Ciotti, A., Dierssen, H., Dowell, M., Dunne, J., Esaias, W., Gentili, B., Gregg, W., Groom, S., Hoepffner, N., Ishizaka, J., Kameda, T., Le Quéré, C., Lohrenz, S., Marra, J., Mélin, F., Moore, K., Morel, A., Reddy, T. E., Ryan, J., Scardi, M., Smyth, T., Turpie, K., Tilstone, G., Waters, K., and Yamanaka, Y.: A comparison of global estimates of marine primary production from ocean color, Deep-Sea Res. Pt. II, 53, 741–770, doi:10.1016/j.dsr2.2006.01.028, 2006.

Chen, C., Liu, H., and Beardsley, R. C.: An unstructured grid, finite-volume, three-dimensional, primitive equations ocean model: application to coastal ocean and estuaries, J. Atmos. Ocean. Tech., 20, 159–186, doi:10.1175/1520-0426(2003)020<0159:AUGFVT>2.0.CO;2, 2003.

Danilov, S., Kivman, G., and Schröter, J.: A finite-element ocean model: principles and evaluation, Ocean Model., 6, 125–150, doi:10.1016/S1463-5003(02)00063-X, 2004.

De Baar, H. J. W., De Jong, J. T. M., Bakker, D. C., Löscher, B. M., Veth, C., Bathmann, U., and Smetacek, V.: Importance of iron for plankton blooms and carbon dioxide drawdown in the Southern Ocean, Nature, 373, doi:10.1038/373412a0, 1995.

de Boyer Montegut, C., Madec, G., Fischer, A. S., Lazar, A., and Iudicone, D.: Mixed layer depth over the global ocean: An examination of profile data and a profile-based climatology, J. Geophys. Res., 109, doi:10.1029/2004JC002378, 2004.

48

Doney, S. C., Lindsay, K., Caldeira, K., Campin, J.-M., Drange, H., Dutay, J.-C., Follows, M., Gao, Y., Gnanadesikan, A., Gruber, N., Ishida, A., Joos, F., Madec, G., Maier-Reimer, E., Marshall, J. C., Matear, R. J., Monfray, P., Mouchet, A., Najjar, R., Orr, J. C., Plattner, G. K., Sarmiento, J. L., Schlitzer, R., Slater, R. D., Totterdell, I. J., Weirig, M. F., Yamanaka, Y., and Yool, A.: Evaluat-
5   ing global ocean carbon models: The importance of realistic physics, Global Biogeochem. Cy., 18, doi:10.1029/2003GB002150, 2004.

Doney, S. C., Lima, I., Moore, J. K., Lindsay, K., Behrenfeld, M. J., Westberry, T. K., Mahowald, N., Glover, D. M., and Takahashi, T.: Skill metrics for confronting global upper ocean ecosystem-biogeochemistry models against field and remote sensing data, J. Marine Syst., 76, 95–112,
10   doi:10.1016/j.jmarsys.2008.05.015, 2009.

Downes, S., Farneti, R., Uotilac, P., Griffies, S. M., Marsland, S., Bailey, D., Behrens, E., Bentsen, M., Bi, D., Biastoch, A., Böning, C., Bozec, A., Chassignet, E., Danabasoglu, G., Danilov, S., Diansky, N., Drange, H., Fogli, P. G., Gusev, A., Howard, A., Illicak, M., Jung, T., Kelley, M., Large, W. G., Leboissetiero, A., Long, M., Lu, J., Masina, S., Mishra, A., Navarra, A., Nurserp, A. J. G., Patara, L.,
15   Samuels, B. L., Sidorenko, D., Spence, P., Tsujino, H., Wang, Q., and Yeager, S. G.: An assessment of Southern Ocean water masses and sea ice during 1988-2007 in a suite of inter-annual CORE-II simulations, Clim. Dynam., submitted.

Droop, M.: 25 Years of Algal Growth Kinetics A Personal View, Bot. mar., 26, 99–112, doi:10.1515/botm.1983.26.3.99, 1983.

20   Dunne, J. P., Sarmiento, J. L., and Gnanadesikan, A.: A synthesis of global particle export from the surface ocean and cycling through the ocean interior and on the seafloor, Global Biogeochem. Cy., 21, doi:10.1029/2006GB002907, 2007.

Elrod, V. A., Berelson, W. M., Coale, K. H., and Johnson, K. S.: The flux of iron from continental shelf sediments: A missing source for global budgets, Geophys. Res. Lett., 31, doi:10.1029/2004GL020216,
25   2004.

Friedrichs, M. A., Carr, M.-E., Barber, R. T., Scardi, M., Antoine, D., Armstrong, R. A., Asanuma, I., Behrenfeld, M. J., Buitenhuis, E. T., Chai, F., Christian, J. R., Ciotti, A. M., Doney, S. C., Dowell, M., Dunne, J., Gentili, B., Gregg, W., Hoepffner, N., Ishizaka, J., Kameda, T., Lima, I., Marra, J., Mélin, F., Moore, J. K., Morel, A., O'Malley, R. T., O'Reilly, J., Saba, V. S., Schmeltz, M.,
30   Smyth, T. J., Tjiputra, J., Waters, K., Westberry, T. K., and Winguth, A.: Assessing the uncertainties of model estimates of primary productivity in the tropical Pacific Ocean, J. Marine Syst., 76, 113–133, doi:10.1016/j.jmarsys.2008.05.010, 2009.

49

Fung, I. Y., Meyn, S. K., Tegen, I., Doney, S. C., John, J. G., and Bishop, J. K. B.: Iron supply and demand in the upper ocean, Global Biogeochem. Cy., 14, 281–295, doi:10.1029/1999GB900059, 2000.

Garcia, H., Locarnini, R., Boyer, T., and Antonov, J.: In World Ocean Atlas 2005, Volume 4: Nutrients (phosphate, nitrate, silicate),(ed. S. Levitus), Tech. rep., NOAA Atlas NESDIS, Washington, DC, 2006.

Garcia, H., Locarnini, R., Boyer, T., Antonov, J., Zweng, M., Baranova, O., and Johnson, D.: World Ocean Atlas 2009, Volume 4: Nutrients (phosphate, nitrate, silicate),(ed. S. Levitus), Tech. rep., NOAA Atlas NESDIS, Washington, DC, 2010.

Geider, R. J., MacIntyre, H. L., and Kana, T. M.: A dynamic model of photoadaptation in phytoplankton, Limnol. Oceanogr., 41, 1–15, 1996.

Geider, R. J., MacIntyre, H. L., and Kana, T. M.: A dynamic regulatory model of phytoplanktonic acclimation to light, nutrients, and temperature, Limnol. Oceanogr., 43, 679–694, doi:10.4319/lo.1998.43.4.0679, 1998.

Gent, P. R. and Mcwilliams, J. C.: Isopycnal mixing in ocean circulation models, Journal of Physical Oceanography, 20, 150–155, doi:10.1175/1520-0485(1981)011<1443:POVMIN>2.0.CO;2, 1990.

Gent, P. R., Yeager, S. G., Neale, R. B., Levis, S., and Bailey, D. A.: Improvements in a half degree atmosphere/land version of the CCSM, Clim. Dynam., 34, 819–833, doi:10.1007/s00382-009-0614-8, 2010.

Gentleman, W., Leising, A., Frost, B., Strom, S., and Murray, J.: Functional responses for zooplankton feeding on multiple resources: a review of assumptions and biological dynamics, Deep-Sea Res. Pt. II, 50, 2847–2875, doi:10.1016/j.dsr2.2003.07.001, 2003.

Gordon, R. M., Coale, K. H., and Johnson, K. S.: Iron distributions in the equatorial Pacific: Implications for new production, Limnol. Oceanogr., 42, 419–431, 1997.

Gregg, W. W. and Casey, N. W.: Global and regional evaluation of the SeaWiFS chlorophyll data set, Remote Sensing of Environment, 93, 463–479, doi:10.1016/j.rse.2003.12.012, 2004.

Griffies, S. M., Biastoch, A., Böning, C., Bryan, F., Danabasoglu, G., Chassignet, E. P., England, M. H., Gerdes, R., Haak, H., Hallberg, R. W., Hazeleger, W., Jungclaus, J., Large, W. G., Madec, G., Pirani, A., Samuels, B. L., Scheinert, M., Gupta, A. S., Severijns, C. A., Simmons, H. L., Treguier, A. M., Winton, M., Yeager, S., and Yin, J.: Coordinated ocean-ice reference experiments (COREs), Ocean Model., 26, 1–46, doi:10.1016/j.ocemod.2008.08.007, 2009.

Haid, V. and Timmermann, R.: Simulated heat flux and sea ice production at coastal polynyas in the southwestern Weddell Sea, J. Geophys. Res, 118, 2640–2652, doi:10.1002/jgrc.20133, 2013.

Hashioka, T., Vogt, M., Yamanaka, Y., Le Quéré, C., Buitenhuis, E. T., Aita, M. N., Alvain, S., Bopp, L., Hirata, T., Lima, I., Sailley, S., and Doney, S. C.: Phytoplankton competition during the spring bloom in four plankton functional type models, Biogeosciences, 10, 6833–6850, doi:10.5194/bg-10-6833-2013, 2013.

Hauck, J., Völker, C., Wang, T., Hoppema, M., Losch, M., and Wolf-Gladrow, D.: Seasonally different carbon flux changes in the Southern Ocean in response to the Southern Annular Mode, Global Biogeochem. Cy., 27, 1–10, doi:10.1002/2013GB004600, 2013.

Hill, J., Popova, E. E., Ham, D. A., Piggott, M. D., and Srokosz, M.: Adapting to life: ocean biogeochemical modelling and adaptive remeshing, Ocean Science, 10, 323–343, doi:10.5194/os-10-323-2014, http://www.ocean-sci.net/10/323/2014/, 2014.

Hirata, T., Hardman-Mountford, N. J., Brewin, R. J. W., Aiken, J., Barlow, R., Suzuki, K., Isada, T., Howell, E., Hashioka, T., Noguchi-Aita, M., and Yamanaka, Y.: Synoptic relationships between surface Chlorophyll-a and diagnostic pigments specific to phytoplankton functional types, Biogeosciences, 8, 311–327, doi:10.5194/bg-8-311-2011, 2011.

Hohn, S.: Coupling and decoupling of biogeochemical cycles in marine ecosystems, Ph.D. thesis, Bremen University, Germany, 2009.

Holzer, M., Primeau, F. W., DeVries, T., and Matear, R.: The Southern Ocean silicon trap: Data-constrained estimates of regenerated silicic acid, trapping efficiencies, and global transport paths, J. Geophys. Res, 119, 313–331, doi:10.1002/2013JC009356, 2014.

Hoppema, M., de Baar, H. J., Fahrbach, E., Hellmer, H. H., and Klein, B.: Substantial advective iron loss diminishes phytoplankton production in the Antarctic Zone, Global Biogeochem. Cy., 17, doi:10.1029/2002GB001957, 2003.

Jakobsson, M., Macnab, R., Mayer, L., Anderson, R., Edwards, M., Hatzky, J., Schenke, H. W., and Johnson, P.: An improved bathymetric portrayal of the Arctic Ocean: Implications for ocean modeling and geological, geophysical and oceanographic analyses, Geophysical Research Letters, 35, 2008.

Jin, X., Gruber, N., Dunne, J. P., Sarmiento, J. L., and Armstrong, R. A.: Diagnosing the contribution of phytoplankton functional groups to the production and export of particulate organic carbon, CaCO3, and opal from global nutrient and alkalinity distributions, Global Biogeochem. Cy., 20, doi:10.1029/2005GB002532, 2006.

Johnson, G. C., McPhaden, M. J., and Firing, E.: Equatorial Pacific Ocean Horizontal Velocity, Divergence, and Upwelling*, J. Phys. Oceanogr., 31, 839–849, doi:10.1175/1520-0485(2001)031<0839:EPOHVD>2.0.CO;2, 2001.

Kamatani, A.: Dissolution rates of silica from diatoms decomposing at various temperatures, Mar. Biol., 68, 91–96, doi:10.1007/BF00393146, 1982.

Key, R. M., Kozyr, A., Sabine, C. L., Lee, K., Wanninkhof, R., Bullister, J. L., Feely, R. A., Millero, F. J., Mordy, C., and Peng, T.-H.: A global ocean carbon climatology: Results from Global Data Analysis Project (GLODAP), Global Biogeochem. Cy., 18, doi:10.1029/2004GB002247, 2004.

Kriest, I. and Oschlies, A.: On the treatment of particulate organic matter sinking in large-scale models of marine biogeochemical cycles, Biogeosciences, 5, 55–72, doi:10.5194/bg-5-55-2008, 2008.

Lam, P. J. and Bishop, J. K.: The continental margin is a key source of iron to the HNLC North Pacific Ocean, Geophys. Res. Lett., 35, doi:10.1029/2008GL033294, 2008.

Lancelot, C., de Montety, A., Goosse, H., Becquevort, S., Schoemann, V., Pasquer, B., and Vancoppenolle, M.: Spatial distribution of the iron supply to phytoplankton in the Southern Ocean: a model study., Biogeosciences, 6, 2861–2878, doi:10.5194/bg-6-2861-2009, 2009.

Large, W. G. and Yeager, S. G.: Diurnal to Decadal Global Forcing for Oceans and Sea-Ice Models: The Data Sets and Flux Climatologies, NCAR/TN-460+STR, Tech. rep., National Center for Atmospheric Research, Boulder, Colorado, 2004.

Large, W. G. and Yeager, S. G.: The global climatology of an interannually varying air–sea flux data set, Clim. Dynam., 33, 341–364, doi:10.1007/s00382-008-0441-3, 2009.

Laws, E. A., Falkowski, P. G., Smith, W. O., Ducklow, H., and McCarthy, J. J.: Temperature effects on export production in the open ocean, Global Biogeochem. Cy., 14, 1231–1246, doi:10.1029/1999GB001229, 2000.

Le Quéré, C., Aumont, O., Monfray, P., and Orr, J.: Propagation of climatic events on ocean stratification, marine biology, and CO_2: Case studies over the 1979–1999 period, J. Geophys. Res, 108, doi:10.1029/2001JC000920, 2003.

Löscher, B. M., De Baar, H. J. W., De Jong, J. T. M., Veth, C., and Dehairs, F.: The distribution of Fe in the Antarctic circumpolar current, Deep-Sea Res. Pt. II, 44, 143–187, doi:10.1016/S0967-0645(96)00101-4, 1997.

Luo, C., Mahowald, N. M., and Del Corral, J.: Sensitivity study of meteorological parameters on mineral aerosol mobilization, transport, and distribution, J. Geophys. Res, 108, doi:10.1029/2003JD003483, 2003.

Mahowald, N., Luo, C., Del Corral, J., and Zender, C. S.: Interannual variability in atmospheric mineral aerosols from a 22-year model simulation and observational data, J. Geophys. Res, 108, doi:10.1029/2002JD002821, 2003.

Martin, J. H., Gordon, R. M., and Fitzwater, S. E.: The case for iron, Limnol. Oceanogr., 36, 1991.

Moore, J. and Braucher, O.: Sedimentary and mineral dust sources of dissolved iron to the world ocean, Biogeosciences, 5, 631–656, doi:10.5194/bg-5-631-2008, 2008.

Moore, J. K., Abbott, M. R., and Richman, J. G.: Location and dynamics of the Antarctic Polar Front from satellite sea surface temperature data, Journal of Geophysical Research: Oceans (1978–2012), 104, 3059–3073, 1999.

Moore, J. K., Doney, S. C., Glover, D. M., and Fung, I. Y.: Iron cycling and nutrient-limitation patterns in surface waters of the World Ocean, Deep-Sea Res. Pt. II, 49, 463–507, doi:10.1016/S0967-0645(01)00109-6, 2002.

Moore, J. K., Doney, S. C., and Lindsay, K.: Upper ocean ecosystem dynamics and iron cycling in a global three-dimensional model, Global Biogeochem. Cy., 18, doi:10.1029/2004GB002220, 2004.

Najjar, R. G., Jin, X., Louanchi, F., Aumont, O., Caldeira, K., Doney, S. C., Dutay, J.-C., Follows, M., Gruber, N., Joos, F., Lindsay, K., Maier-Reimer, E., Matear, R. J., Matsumoto, K., Monfray, P., Mouchet, A., Orr, J. C., Plattner, G.-K., Sarmiento, J. L., Schlitzer, R., Slater, R. D., Weirig, M.-F., Yamanaka, Y., and Yool, A.: Impact of circulation on export production, dissolved organic matter, and dissolved oxygen in the ocean: Results from Phase II of the Ocean Carbon-cycle Model Intercomparison Project (OCMIP-2), Global Biogeochem. Cy., 21, doi:10.1029/2006GB002857, 2007.

Nevison, C., Keeling, R., Kahru, M., Manizza, M., Mitchell, B., and Cassar, N.: Estimating net community production in the Southern Ocean based on atmospheric potential oxygen and satellite ocean color data, Global Biogeochem. Cy., 26, doi:10.1029/2011GB004040, 2012.

Orr, J., Najjar, R., Sabine, C. L., and Joos, F.: Abiotic-HOWTO, Tech. rep., Internal OCMIP Report, LSCE/CEA Saclay, Gif-sur-Yvette, France, 1999.

Pacanowski, R. and Philander, S.: Parameterization of vertical mixing in numerical models of tropical oceans, Journal of Physical Oceanography, 11, 1443–1451, doi:10.1175/1520-0485(1981)011<1443:POVMIN>2.0.CO;2, 1981.

Parekh, P., Follows, M. J., and Boyle, E. A.: Decoupling of iron and phosphate in the global ocean, Global Biogeochem. Cy., 19, doi:10.1029/2004GB002280, 2005.

Parkinson, C. L. and Washington, W. M.: A large-scale numerical model of sea ice, Journal of Geophysical Research: Oceans, 84, 311–337, doi:10.1029/JC084iC01p00311, 1979.

Piggott, M. D., Gorman, G. J., Pain, C. C., Allison, P. A., Candy, A. S., Martin, B. T., and Wells, M. R.: A new computational framework for multi-scale ocean modelling based on adapting unstructured meshes, Int. J. Numer. Meth. Fl., 56, 1003–1015, doi:10.1002/fld.1663, 2008.

Redi, M. H.: Oceanic isopycnal mixing by coordinate rotation, Journal of Physical Oceanography, 12, 1154–1158, doi:10.1175/1520-0485(1982)012<1154:OIMBCR>2.0.CO;2, 1982.

Schlitzer, R.: Carbon export fluxes in the Southern Ocean: Results from inverse modeling and comparison with satellite-based estimates, Deep-Sea Res. Pt. II, 49, 1623–1644, doi:10.1016/S0967-0645(02)00004-8, 2002.

Schlitzer, R.: Export production in the equatorial and North Pacific derived from dissolved oxygen, nutrient and carbon data, Journal of Oceanography, 60, 53–62, doi:10.1023/B:JOCE.0000038318.38916.e6, 2004.

Schneider, B., Bopp, L., Gehlen, M., Segschneider, J., Frölicher, T. L., Cadule, P., Friedlingstein, P., Doney, S. C., Behrenfeld, M. J., and Joos, F.: Climate-induced interannual variability of marine primary and export production in three global coupled climate carbon cycle models, Biogeosciences, 5, 597–614, doi:10.5194/bg-5-597-2008, 2008.

Sidorenko, D., Danilov, S., Wang, Q., Huerta-Casas, A., and Schröter, J.: On computing transports in finite-element models, Ocean Modelling, 28, 60–65, doi:10.1016/j.ocemod.2008.09.001, 2009.

Sidorenko, D., Wang, Q., Danilov, S., and Schröter, J.: FESOM under coordinated ocean-ice reference experiment forcing, Ocean Dynam., 61, 881–890, doi:10.1007/s10236-011-0406-7, 2011.

Siegel, D. A., Buesseler, K. O., Doney, S. C., Sailley, S. F., Behrenfeld, M. J., and Boyd, P. W.: Global assessment of ocean carbon export by combining satellite observations and food-web models, Global Biogeochemical Cycles, 28, 181–196, doi:10.1002/2013GB004743, http://dx.doi.org/10.1002/2013GB004743, 2014.

Steele, M., Morley, R., and Ermold, W.: PHC: A global ocean hydrography with a high-quality Arctic Ocean, J. Climate, 14, 2079–2087, doi:10.1029/2006GL026152, 2001.

Steinacher, M., Joos, F., Frölicher, T. L., Bopp, L., Cadule, P., Cocco, V., Doney, S. C., Gehlen, M., Lindsay, K., Moore, J. K., Schneider, B., and Segschneider, J.: Projected 21st century decrease in marine productivity: a multi-model analysis, Biogeosciences, 7, 979–1005, doi:10.5194/bg-7-979-2010, 2010.

Sunda, W. G. and Huntsman, S. A.: Iron uptake and growth limitation in oceanic and coastal phytoplankton, Marine Chemistry, 50, 189–206, doi:10.1016/0304-4203(95)00035-P, 1995.

Tagliabue, A., Mtshali, T., Aumont, O., Bowie, A. R., Klunder, M. B., Roychoudhury, A. N., and Swart, S.: A global compilation of dissolved iron measurements: focus on distributions and processes in the Southern Ocean, Biogeosciences, 9, 1–17, doi:10.5194/bg-9-2333-2012, 2012.

Tagliabue, A., Sallée, J.-B., Bowie, A. R., Lévy, M., Swart, S., and Boyd, P. W.: Surface-water iron supplies in the Southern Ocean sustained by deep winter mixing, Nat. Geosci., 7, 314–320, doi:10.1038/ngeo2101, 2014.

54

Taylor, K. E.: Summarizing multiple aspects of model performance in a single diagram, J. Geophys. Res, 106, 7183–7192, doi:10.1029/2000JD900719, 2001.

Taylor, M. H., Losch, M., and Bracher, A.: On the drivers of phytoplankton blooms in the Antarctic marginal ice zone: A modeling approach, J. Geophys. Res, 118, 63–75, doi:10.1029/2012JC008418, 2013.

Timmermann, R., Danilov, S., Schröter, J., Böning, C., Sidorenko, D., and Rollenhagen, K.: Ocean circulation and sea ice distribution in a finite element global sea ice–ocean model, Ocean Model., 27, 114–129, doi:10.1016/j.ocemod.2008.10.009, 2009.

Timmermann, R., Le Brocq, A. M., Deen, T. J., Domack, E. W., Dutrieux, P., Galton-Fenzi, B., Hellmer, H. H., Humbert, A., Jansen, D., Jenkins, A., Lambrecht, A., Makinson, K., Niederjasper, F., Nitsche, F.-O., N?st, O. A., Smedsrud, L. H., and Smith, W.: Antarctic ice sheet topography, cavity geometry, and global bathymetry (RTopo 1.0.5-beta), doi:10.1594/PANGAEA.741917, http://doi.pangaea.de/10.1594/PANGAEA.741917, 2010.

Vichi, M. and Masina, S.: Skill assessment of the PELAGOS global ocean biogeochemistry model over the period 1980–2000, Biogeosciences, 6, 2333–2353, doi:10.5194/bg-6-2333-2009, 2009.

Vogt, M., Hashioka, T., Payne, M. R., Buitenhuis, E. T., Quéré, C. L., Alvain, S., Aita, M. N., Bopp, L., Doney, S. C., Hirata, T., Lima, I., Sailley, S., and Yamanaka, Y.: The distribution, dominance patterns and ecological niches of plankton functional types in Dynamic Green Ocean Models and satellite estimates, Biogeosciences Discuss., 10, 17 193–17 247, doi:10.5194/bgd-10-17193-2013, 2013.

Wagener, T., Guieu, C., Losno, R., Bonnet, S., and Mahowald, N.: Revisiting atmospheric dust export to the Southern Hemisphere ocean: Biogeochemical implications, Global Biogeochem. Cy., 22, doi:10.1029/2007GB002984, 2008.

Wang, Q., Danilov, S., and Schröter, J.: Finite element ocean circulation model based on triangular prismatic elements, with application in studying the effect of topography representation, J. Geophys. Res, 113, doi:10.1029/2007JC004482, 2008.

Wang, Q., Danilov, S., Sidorenko, D., Timmermann, R., Wekerle, C., Wang, X., Jung, T., and Schröter, J.: The Finite Element Sea Ice-Ocean Model (FESOM) v.1.4: formulation of an ocean general circulation model, Geoscientific Model Development, 7, 663–693, doi:10.5194/gmd-7-663-2014, 2014a.

Wang, S., Bailey, D., Lindsay, K., Moore, K., and Holland, M.: Impacts of sea ice on the marine iron cycle and phytoplankton productivity, Biogeosciences Discuss., 11, 2383–2418, doi:10.5194/bgd-11-2383-2014, 2014b.

Wanninkhof, R.: Relationship between wind speed and gas exchange over the ocean, J. Geophys. Res, 97, 7373–7382, doi:10.1029/92JC00188, 1992.

Wekerle, C., Wang, Q., Danilov, S., Jung, T., and Schröter, J.: The Canadian Arctic Archipelago through-flow in a multiresolution global model: Model assessment and the driving mechanism of interannual variability, J. Geophys. Res, 118, 4525–4541, doi:10.1002/jgrc.20330, 2013.

Wilhelm, S. W., King, A. L., Twining, B. S., LeCleir, G. R., DeBruyn, J. M., Strzepek, R. F., Breene, C. L., Pickmere, S., Ellwood, M. J., Boyd, P. W., et al.: Elemental quotas and physiology of a south-western Pacific Ocean plankton community as a function of iron availability, Aquat. Microb. Ecol., 68, 185–194, doi:10.3354/ame01611, 2013.

Wolf-Gladrow, D. A., Zeebe, R. E., Klaas, C., Körtzinger, A., and Dickson, A. G.: Total alkalinity: The explicit conservative expression and its application to biogeochemical processes, Marine Chemistry, 106, 287–300, 2007.

Yamanaka, Y. and Tajika, E.: The role of the vertical fluxes of particulate organic matter and calcite in the oceanic carbon cycle: Studies using an ocean biogeochemical general circulation model, Global Biogeochem. Cy., 10, 361–382, doi:10.1029/96GB00634, 1996.

Yool, A., Popova, E. E., and Anderson, T. R.: Medusa-1.0: a new intermediate complexity plankton ecosystem model for the global domain, Geosci. Model Dev., 4, 381–417, doi:10.5194/gmd-4-381-2011, 2011.

Table 1. List of the observational data sets used for the skill assessment.

Data set	Variable Name	Temporal coverage	Reference
Sea surface temperature	SST	Monthly climatology	Garcia et al. (2010)
Sea surface salinity	SSS	Monthly climatology	Garcia et al. (2010)
Mixed layer depth	MLD	Monthly climatology	de Boyer Montegut et al. (2004)
Dissolved inorganic nitrogen	DIN	Monthly climatology	Garcia et al. (2010)
Dissolved inorganic silicon	DSi	Monthly climatology	Garcia et al. (2010)
Chlorophyll a concentration	Chl	Monthly (1998–2010)	www.globcolour.info
Net primary production	NPP	Monthly (2003–2008)	SeaWIFS and Behrenfeld and Falkowski (1997) http://www.science.oregonstate.edu/ocean.productivity/index.php
Export production	EP	Annual climatologies	Schlitzer (2004); Laws et al. (2000)
test	test	Three Drie	test

Table 2. Modelled mean surface iron concentrations (0–100 m) in the different ocean basins shown in Fig. 3. Observed values are from Moore and Braucher (2008), except those marked with *, which are from Tagliabue et al. (2012), Table 2. The latter is the mean of the values given for the Antarctic and Subantarctic regions.

Basin	Latitudinal extent	Model [nM]	Obs [nM]
North Atlantic	45–70° N	0.34	
North-central Atlantic	10–45° N	1.03	0.68
South-central Atlantic	45–10° S	0.28	0.44
North Indian	45–10° S	1.10	1.21
North Pacific	45–70° N	0.14	0.31
Equatorial Pacific	10° S–10° N	0.02	0.84
South-central Pacific	45–10° S	0.02	0.31
Atlantic Southern Ocean	90–45° S	0.14	0.39*
Indian Southern Ocean	90–45° S	0.08	0.33*
Pacific Southern Ocean	90–45° S	0.09	0.15*

Table 3. Net primary and export production for the global domain and the Southern Ocean south of $50°$ S, for REcoM2 and from literature.

	Units	REcoM2-FESOM	Previous studies
NPP_{glo}	$[Pg\,C\,yr^{-1}]$	32.5	35–70 (Carr et al., 2006) 23.7 - 30.7 (Schneider et al., 2008) 47.3 (SeaWIFS and Behrenfeld and Falkowski, 1997)
EP_{glo}	$[Pg\,C\,yr^{-1}]$	6.1	5.8–13.0 (Dunne et al., 2007) 6 (Siegel et al., 2014)
$Opal_{glo}$	$[Tmol\,Si\,yr^{-1}]$	74.5	69–185 (Dunne et al., 2007)
NPP_{SO}	$[Pg\,C\,yr^{-1}]$	3.1	1.1–4.9 (Carr et al., 2006)
EP_{SO}	$[Pg\,C\,yr^{-1}]$	1.1	1 (Schlitzer, 2002; Nevison et al., 2012)
$Opal_{SO}$	$[Tmol\,Si\,yr^{-1}]$	21.5	21–54 (Dunne et al., 2007)

Table 4. State variables, ocean.

Variable	Description and unit
DIN	Dissolved Inorganic Nitrogen $[\mathrm{mmol\,N\,m^{-3}}]$
DSi	Dissolved Inorganic Silicon $[\mathrm{mmol\,N\,m^{-3}}]$
DFe	Dissolved Inorganic Iron $[\mathrm{\mu mol\,Fe\,m^{-3}}]$
DIC	Dissolved Inorganic Carbon $[\mathrm{mmol\,C\,m^{-3}}]$
Alk	Alkalinity $[\mathrm{mmol\,C\,m^{-3}}]$
$\mathrm{PhyN_{nano}}$	Intracellular nitrogen concentration in nanophytoplankton $[\mathrm{mmol\,N\,m^{-3}}]$
$\mathrm{PhyC_{nano}}$	Intracellular carbon concentration in nanophytoplankton $[\mathrm{mmol\,C\,m^{-3}}]$
PhyCalc	Intracellular calcite concentration in nanophytoplankton $[\mathrm{mmol\,CaCO_3\,m^{-3}}]$
$\mathrm{PhyChl_{nano}}$	Intracellular chl a concentration in nanophytoplankton $[\mathrm{mg\,Chl\,m^{-3}}]$
$\mathrm{PhyN_{dia}}$	Intracellular nitrogen concentration in diatoms $[\mathrm{mmol\,N\,m^{-3}}]$
$\mathrm{PhyC_{dia}}$	Intracellular carbon concentration in diatoms $[\mathrm{mmol\,C\,m^{-3}}]$
$\mathrm{PhySi_{dia}}$	Intracellular silicon concentration in diatoms $[\mathrm{mmol\,Si\,m^{-3}}]$
$\mathrm{PhyChl_{dia}}$	Intracellular chl a concentration in diatoms $[\mathrm{mg\,Chl\,m^{-3}}]$
ZooN	Zooplankton nitrogen concentration $[\mathrm{mmol\,N\,m^{-3}}]$
ZooC	Zooplankton carbon concentration $[\mathrm{mmol\,C\,m^{-3}}]$
DetN	Detritus nitrogen concentration $[\mathrm{mmol\,N\,m^{-3}}]$
DetC	Detritus carbon concentration $[\mathrm{mmol\,C\,m^{-3}}]$
DetCalc	Detritus calcite concentration $[\mathrm{mmol\,CaCO_3\,m^{-3}}]$
DetSi	Detritus silicon concentration $[\mathrm{mmol\,Si\,m^{-3}}]$
DON	Extracellular dissolved organic nitrogen $[\mathrm{mmol\,N\,m^{-3}}]$
DOC	Extracellular dissolved organic carbon $[\mathrm{mmol\,C\,m^{-3}}]$

Table 5. State variables, benthos.

Variable	Description and unit
BenthosN	Benthos, vertically integrated N concentration $[\mathrm{mmol\,N\,m^{-2}}]$
BenthosC	Benthos, vertically integrated C concentration $[\mathrm{mmol\,C\,m^{-2}}]$
BenthosSi	Benthos, vertically integrated Si concentration $[\mathrm{mmol\,Si\,m^{-2}}]$
BenthosCalc	Benthos, vertically integrated calcite concentration $[\mathrm{mmol\,CaCO_3\,m^{-2}}]$

Table 6. Degradation parameters for sources-minus-sinks equations.

Parameter	Value	Description and Unit
ϵ_N^{phy}	0.05	Phytoplankton excretion of organic N [day^{-1}]
ϵ_C^{phy}	0.1	Phytoplankton excretion of organic C [day^{-1}]
ϵ_N^{zoo}	0.1	Zooplankton excretion of organic N [day^{-1}]
ϵ_C^{zoo}	0.1	Zooplankton excretion of organic C [day^{-1}]
ρ_N^{ben}	0.005	Remineralization rate for benthos N [day^{-1}]
ρ_{Si}^{ben}	0.005	Remineralization rate for benthos Si [day^{-1}]
ρ_C^{ben}	0.005	Remineralization rate for benthos C [day^{-1}]
ρ_N	0.11	Temperature dependent remineralization of DON [day^{-1}]
ρ_C	0.1	Temperature dependent remineralization of DOC [day^{-1}]
ρ_{Si}	0.02	Temperature dependent remineralization of DetSi [day^{-1}]
ρ_{DetN}	0.165	Temperature dependent degradation of DetN [day^{-1}]
ρ_{DetC}	0.15	Temperature dependent degradation of DetN [day^{-1}]
deg_{Chl}	0.3	Chlorophyll a degradation rate [day^{-1}]

Table 7. Model variables.

Variable	Description and unit
Agg	Aggregation rate $[\text{day}^{-1}]$
$\text{Diss}_{\text{Calc}}$	Dissolution of calcium carbonate $[\text{day}^{-1}]$
Fe'	Concentration of free iron $[\mu\text{mol}\,\text{Fe}\,\text{m}^{-3}]$
f_T	Temperature dependence of rates, dimensionless
G_{tot}	Total zooplankton grazing rate $[\text{mmol}\,\text{N}\,\text{m}^{-3}\,\text{day}^{-1}]$
G_{nano}	Nanophytoplankton specific zooplankton grazing rate $[\text{mmol}\,\text{N}\,\text{m}^{-3}\,\text{day}^{-1}]$
G_{dia}	Diatom specific zooplankton grazing rate $[\text{mmol}\,\text{N}\,\text{m}^{-3}\,\text{day}^{-1}]$
PAR	Photosynthetically Available Radiation $[\text{W}\,\text{m}^{-2}]$
$P_{\text{nano}}, P_{\text{dia}}$	C-specific actaul rate of photosynthesis $[\text{day}^{-1}]$
P_{max}	C-specific light saturated rate of photosynthesis $[\text{day}^{-1}]$
$r_{\text{nano}}, r_{\text{dia}}$	Phytoplankton respiration rate $[\text{day}^{-1}]$
r_{zoo}	Zooplankton respiration rate $[\text{day}^{-1}]$
ρ_{Si}^{T}	Temperature dependent remineralization rate of Si $[\text{day}^{-1}]$
$S_{\text{nano}}^{\text{chl}}, S_{\text{dia}}^{\text{chl}}$	Rate of chlorophyll a synthesis $[\text{mg}\,\text{Chl}\,\text{mmol}\,\text{C}^{-1}\,\text{d}^{-1}]$
T	Local temperature [K]
$V_{\text{nano}}^{\text{N}}, V_{\text{dia}}^{\text{N}}$	N-assimilation $[\text{mmol}\,\text{N}\,\text{mmol}\,\text{C}^{-1}\,\text{day}^{-1}]$
V^{Si}	Si-assimilation $[\text{mmol}\,\text{Si}\,\text{mmol}\,\text{C}^{-1}\,\text{day}^{-1}]$
w_{det}	Sinking velocity of detritus $[\text{m/day}]$

Table 8. Benthos variables.

Variable	Description and unit
BenF_{Alk}	Flux of alkalinity from benthos to bottom water $[\text{mmol}\,\text{m}^{-2}\,\text{day}^{-1}$
$\text{BenF}_{\text{Calc}}$	Flux of calcite from benthos to bottom water $[\text{mmol}\,\text{CaCO}_3\,\text{m}^{-2}\,\text{day}^{-1}]$
BenF_{DIC}	Flux of C from benthos to bottom water $[\text{mmol}\,\text{C}\,\text{m}^{-2}\,\text{day}^{-1}]$
BenF_{DIN}	Flux of N from benthos to bottom water $[\text{mmol}\,\text{N}\,\text{m}^{-2}\,\text{day}^{-1}]$
BenF_{DSi}	Flux of Si from benthos to bottom water $[\text{mmol}\,\text{Si}\,\text{m}^{-2}\,\text{day}^{-1}]$
BenF_{Fe}	Flux of Fe from benthos to bottom water $[\mu\text{mol}\,\text{Fe}\,\text{m}^{-2}\,\text{day}^{-1}]$
$\text{BenF}_{\text{DetCalc}}$	Flux of detritus calcite from the water to the benthos $[\text{mmol}\,\text{CaCO}_3\,\text{m}^{-2}\,\text{day}^{-1}]$
$\text{BenF}_{\text{DetC}}$	Flux of detritus C from the water to the benthos $[\text{mmol}\,\text{C}\,\text{m}^{-2}\,\text{day}^{-1}]$
$\text{BenF}_{\text{DetN}}$	Flux of detritus N from the water to the benthos $[\text{mmol}\,\text{N}\,\text{m}^{-2}\,\text{day}^{-1}]$
$\text{BenF}_{\text{DetSi}}$	Flux of detritus Si from the water to the benthos $[\text{mmol}\,\text{Si}\,\text{m}^{-2}\,\text{day}^{-1}]$

Table 9. Parameters for iron calculations.

Parameter	Value	Description and Unit
$q^{\text{Fe:C}}$	0.005	Intracellular Fe : C ratio [μmol Fe mmol C^{-1}]
K_{Fe_L}	100.0	Iron stability constant [m^{-3} μmol]
L_{T}	1.0	Total ligand concentration [μmol m^{-3}]
κ_{Fe}	0.0312	Scavenging rate of iron [m^3 mmol C^{-1} day^{-1}]
$q_{\text{sed}}^{\text{Fe:C}}$	0.011	Fe : C ratio for remineralization of Fe from benthos [μmol Fe mmol C^{-1}]

Table 10. Parameters for sources-minus-sinks equations.

Parameter	Value	Description and Unit
ψ	0.1	Calcite production ratio, dimensionless
γ	0.3	Fraction of grazing flux to zooplankton pool, dimensionless
m_{zoo}	0.05	Zooplankton mortality rate $[\text{m}^3\,\text{mmol}\,\text{N}^{-1}\,\text{day}^{-1}]$
ϕ_{phy}	0.02	Max aggregation loss parameter for phytoplankton N $[\text{m}^3\,\text{mmol}\,\text{N}^{-1}\,\text{day}^{-1}]$
ϕ_{det}	0.22	Max aggregation loss parameter for detritus N $[\text{m}^3\,\text{mmol}\,\text{N}^{-1}\,\text{day}^{-1}]$
w_0	20.0	Detritus sinking speed at surface $[\text{m}\,\text{day}^{-1}]$

Table 11. Parameters for phytoplankton growth.

Parameter	Value	Description and Unit
α_{nano}	0.19	Light harvesting efficiency for nanophytoplankton $[\mathrm{mmol\,C\,m^2\,(mg\,Chl\,W\,day)^{-1}}]$
α_{dia}	0.23	Light harvesting efficiency for diatoms $[\mathrm{mmol\,C\,m^2\,(mg\,Chl\,W\,day)^{-1}}]$
$K_{\mathrm{N}}^{\mathrm{Nano}}$	0.55	Half saturation constant for nanophyto N uptake $[\mathrm{mmol\,N\,m^{-3}}]$
$K_{\mathrm{N}}^{\mathrm{Dia}}$	1.00	Half saturation constant for diatom N uptake $[\mathrm{mmol\,N\,m^{-3}}]$
K_{Si}	4.00	Half saturation constant for diatom Si uptake $[\mathrm{mmol\,Si\,m^{-3}}]$
$\mu_{\mathrm{C}}^{\mathrm{max}}$	3.0	Rate of C-specific photosynthesis $[\mathrm{day^{-1}}]$
$q_{\mathrm{max}}^{\mathrm{Chl:N}}$	4.2	Maximum Chl:N ratio for phytoplankton $[\mathrm{mg\,Chl\,mmol\,N^{-1}}]$
res	0.01	Maintenance respiration rate constant $[\mathrm{day^{-1}}]$
$\sigma_{\mathrm{N:C}}$	0.2	Maximum uptake ratio $\mathrm{N:C}$ $[\mathrm{mmol\,N\,mmol\,C^{-1}}]$
$\sigma_{\mathrm{Si:C}}$	0.2	Maximum uptake ratio $\mathrm{Si:C}$ $[\mathrm{mmol\,Si\,mmol\,C^{-1}}]$
τ	0.01	Time scale for zooplankton respiration $[\mathrm{day^{-1}}]$
V_{cm}	0.7	scaling factor for C-specific N-uptake, dimensionless
ζ	2.33	Cost of biosynthesis of N $[\mathrm{mmol\,C\,mmol\,N^{-1}}]$

Table 12. Parameters for grazing.

Parameter	Value	Description and Unit
f_Z^{dia}	0.50	Relative grazing preference for diatoms, dimensionless
G_{max}	2.40	Maximum grazing rate at $0\,^{\circ}\mathrm{C}$ $[\mathrm{day}^{-1}]$
K_G	0.35	Half saturation constant for grazing loss $[(\mathrm{mmol\,N\,m^{-3}})^2]$

68

Table 13. Parameters for limitation functions.

Parameter	Value	Description and Unit
$K_{\mathrm{Fe}}^{\mathrm{nano}}$	0.04	Half saturation constant for nanophytoplankton Fe uptake [$\mu\mathrm{mol\,Fe\,m^{-3}}$]
$K_{\mathrm{Fe}}^{\mathrm{dia}}$	0.12	Half saturation constant for diatom Fe uptake [$\mu\mathrm{mol\,Fe\,m^{-3}}$]
$q^{\mathrm{N:Cmin}}$	0.04	Min intracellular N : C ratio for nanophytoplankton [$\mathrm{mmol\,N\,mmol\,C^{-1}}$]
$q^{\mathrm{N:Cmax}}$	0.2	Max intracellular N : C ratio for nanophytoplankton [$\mathrm{mmol\,N\,mmol\,C^{-1}}$]
$q^{\mathrm{Si:Cmin}}$	0.04	Min intracellular Si : C ratio for diatoms [$\mathrm{mmol\,Si\,mmol\,C^{-1}}$]
$q^{\mathrm{Si:Cmax}}$	0.8	Max intracellular Si : C ratio for diatoms [$\mathrm{mmol\,Si\,mmol\,C^{-1}}$]
$\mathrm{slope}_{\mathrm{min}}^{\mathrm{N}}$	50	Minimum limiter regulater for N, [$\mathrm{mmol\,C\,mmol\,N^{-1}}$]
$\mathrm{slope}_{\mathrm{max}}^{\mathrm{N}}$	1000	Maximum limiter regulater for N, [$\mathrm{mmol\,C\,mmol\,N^{-1}}$]
$\mathrm{slope}_{\mathrm{min}}^{\mathrm{Si}}$	1000	Minimum limiter regulater for Si, [$\mathrm{mmol\,C\,mmol\,N^{-1}}$]
$\mathrm{slope}_{\mathrm{max}}^{\mathrm{Si}}$	1000	Maximum limiter regulater for Si, [$\mathrm{mmol\,C\,mmol\,N^{-1}}$]
T_{ref}	288.15	Reference temperature for Arrhenius function [K]

Table 14. Processes modulated by the limiter function $f_{\text{lim}}^{\text{N:Cmax}}$.

Process	Effect of $q^{\text{N:C}} \to q_{\text{N:Cmax}}$
Nitrogen assimilation	Ends uptake of N
Silicon assimilation	Ends uptake of Si
Respiration by phytoplankton	Ends release of C
Phytoplankton DOC excretion	Ends release of C
Phytoplankton DON excretion	Ends release of N
Phytoplankton calcite excretion	Ends release of C
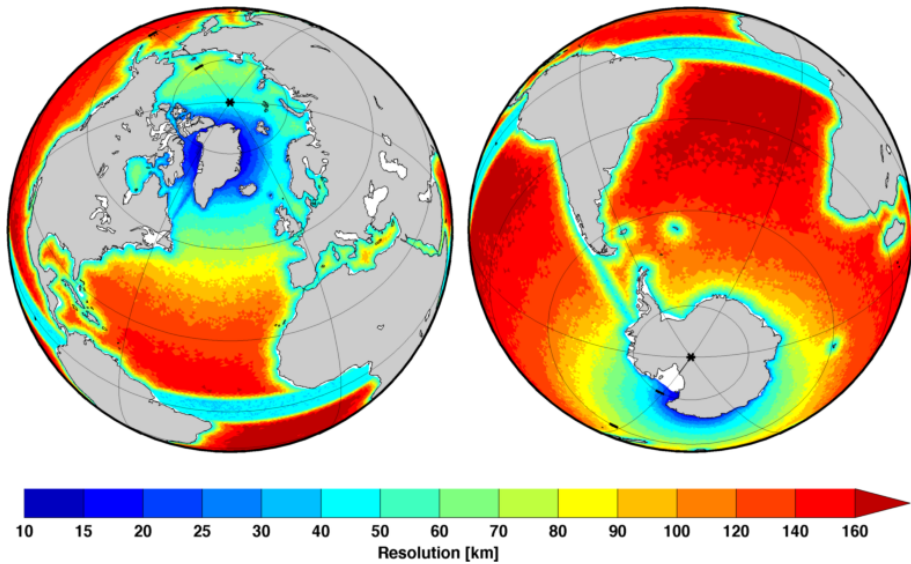
Fig. 1. Horizontal resolution of FESOM's unstructured grid.
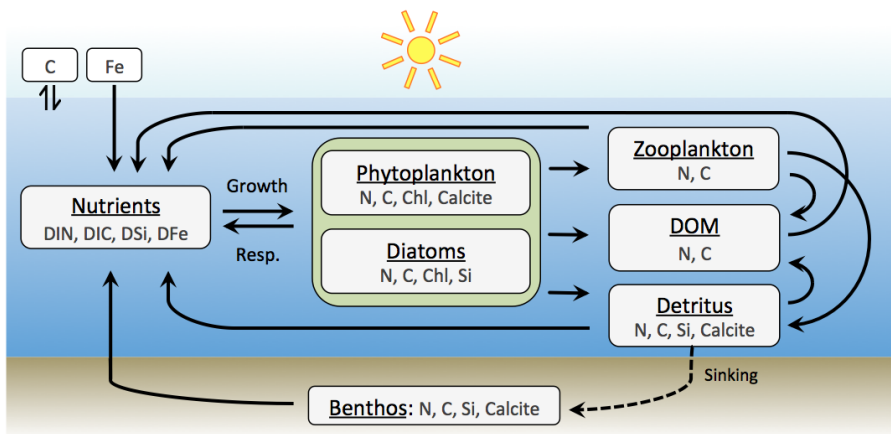
Fig. 2. The pathways in the biogeochemical model REcoM2.
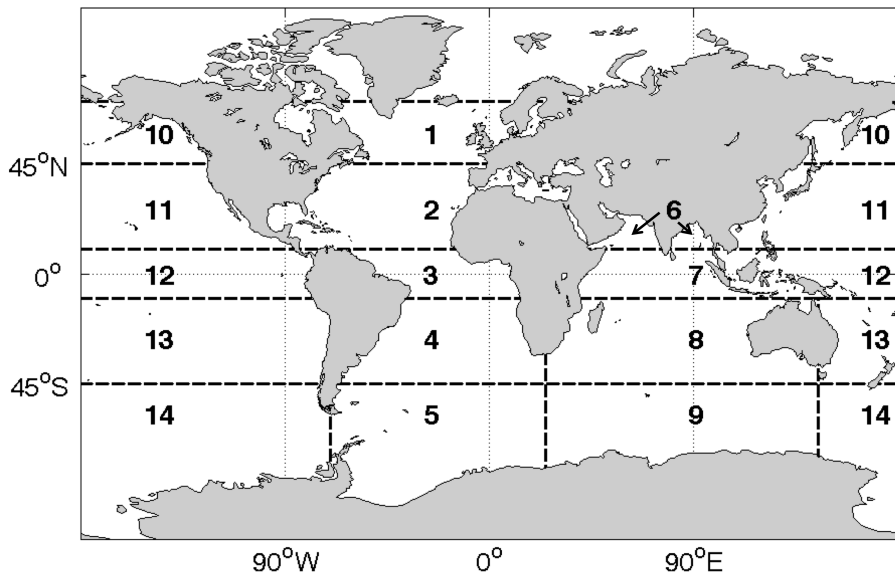
Fig. 3. Map of the ocean regions used to examine the model results on basin scale.
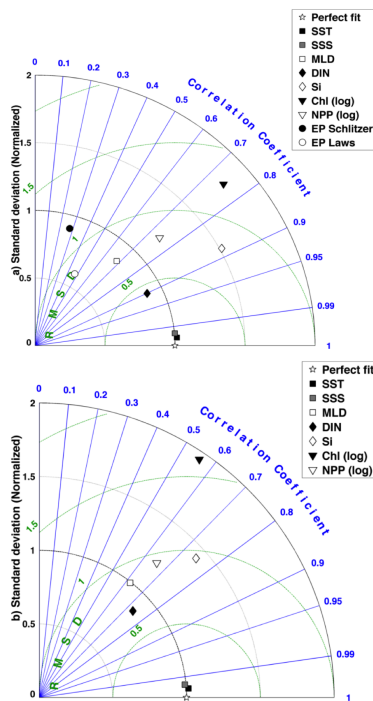
Fig. 4. Taylor diagrams (Taylor, 2001) showing correlation, normalized standard deviation and the normalized root mean square error between values of the model results and observations (Table 1), weighted by area. **(a)** Spatial distribution. **(b)** Spatial-seasonal distribution. All values are surface values, except the mixed layer depth and the vertically integrated NPP. **(a)** Uses the yearly mean calculated over 2004 to 2008 and **(b)** uses the monthly means of the same years. All fields have been interpolated to a 1° by 1° grid, using linear interpolation.
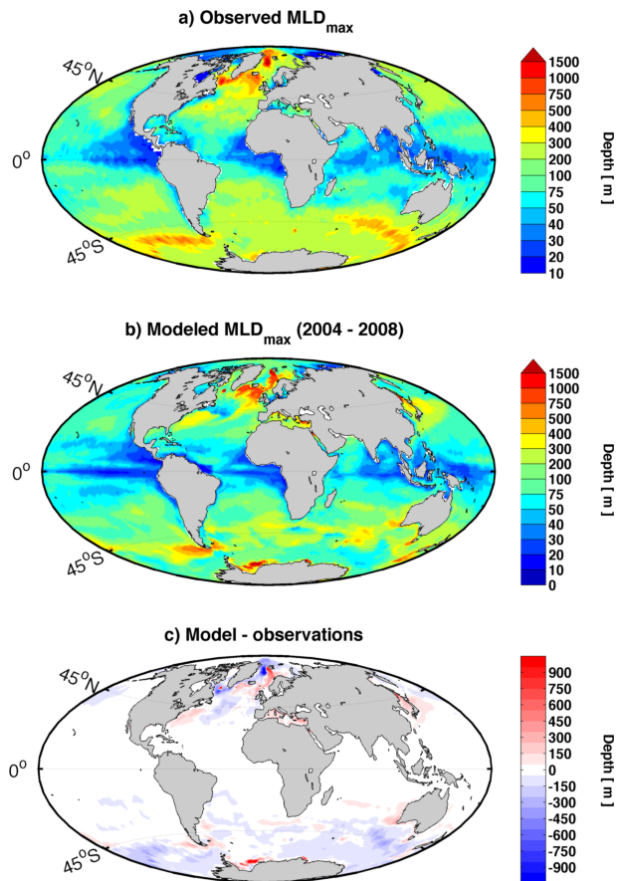
Fig. 5. Mean spatial distribution of the MLD_{max} over the years 2004 to 2008. **(a)** Observation based (de Boyer Montegut et al., 2004). **(b)** Modelled. **(c)** Residual: Modelled – observation based.
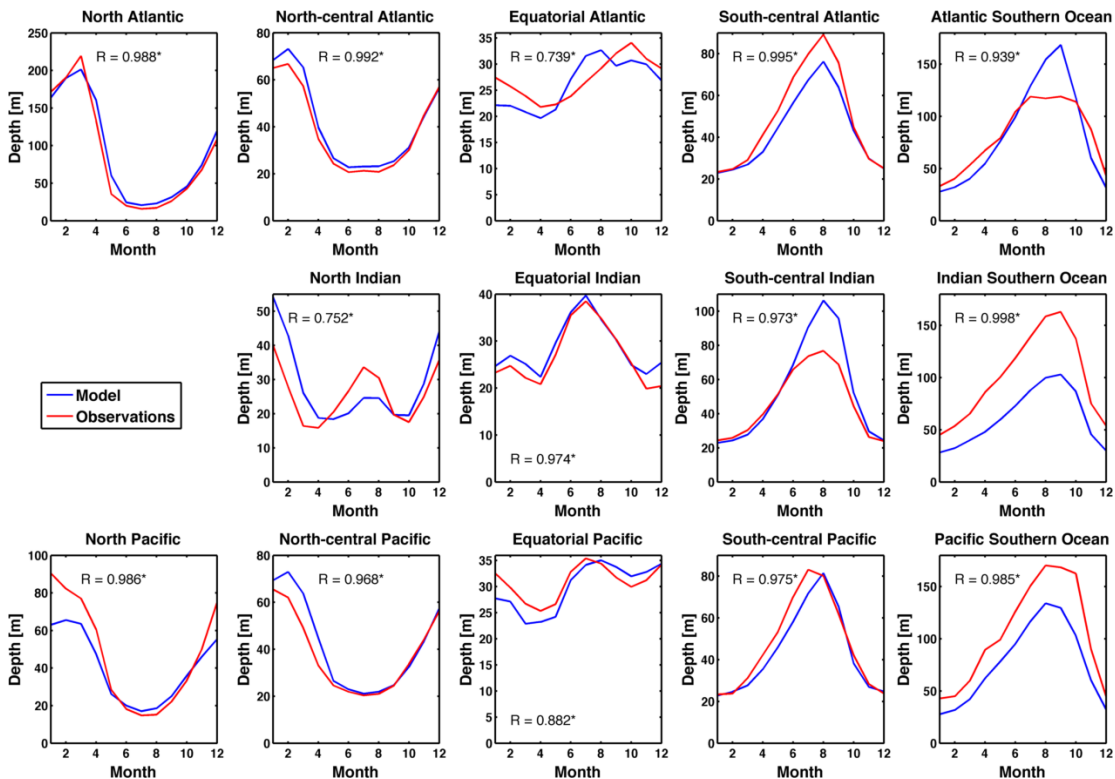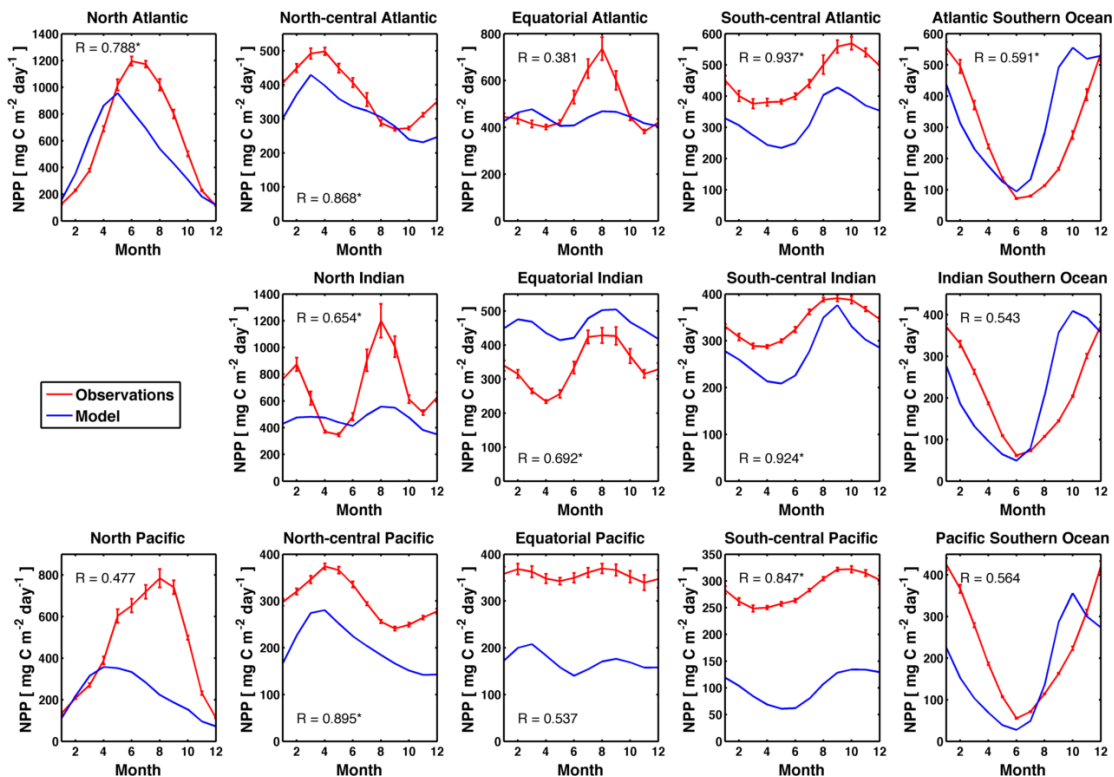
Fig. 6. Mean MLD over the year in the ocean basins depicted in Fig. 3. The correlation coefficient is written in each plot, and the statistically significant correlations (p values < 0.05) are marked with *.
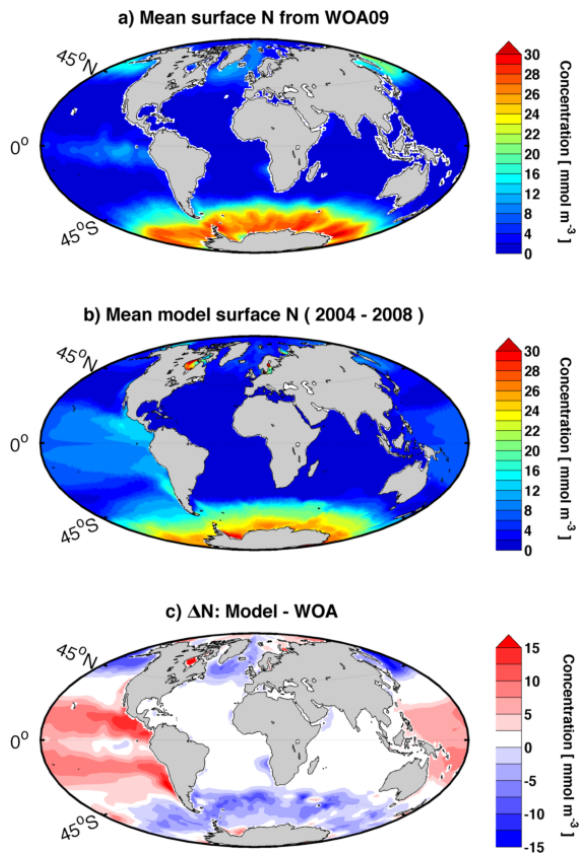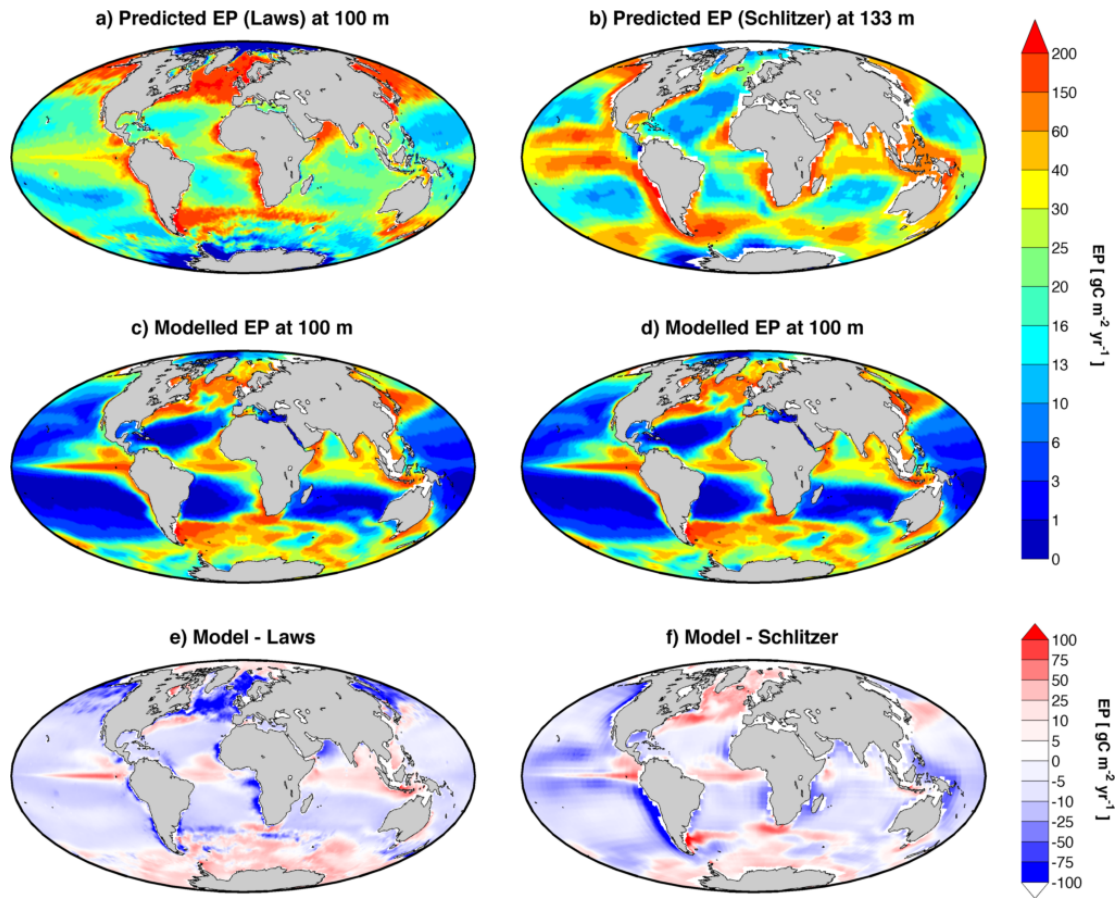
Fig. 7. Spatial distribution of mean surface concentration of dissolved inorganic nitrogen. **(a)** Observed (Garcia et al., 2010) **(b)** Modelled. **(c)** Residual: Modelled – observed.
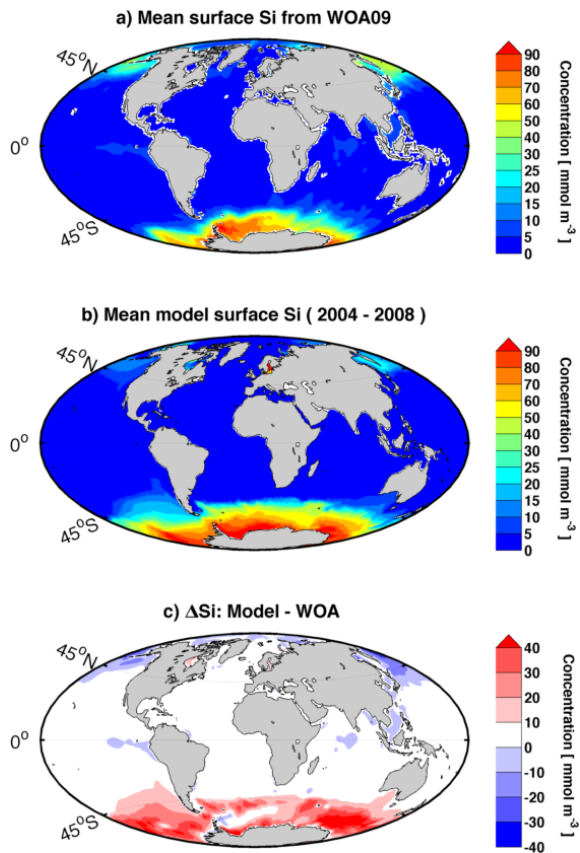
Fig. 8. Spatial distribution of mean surface concentration of dissolved inorganic silicon. **(a)** Observed (Garcia et al., 2010) **(b)** Modelled. **(c)** Residual: Modelled – observed.
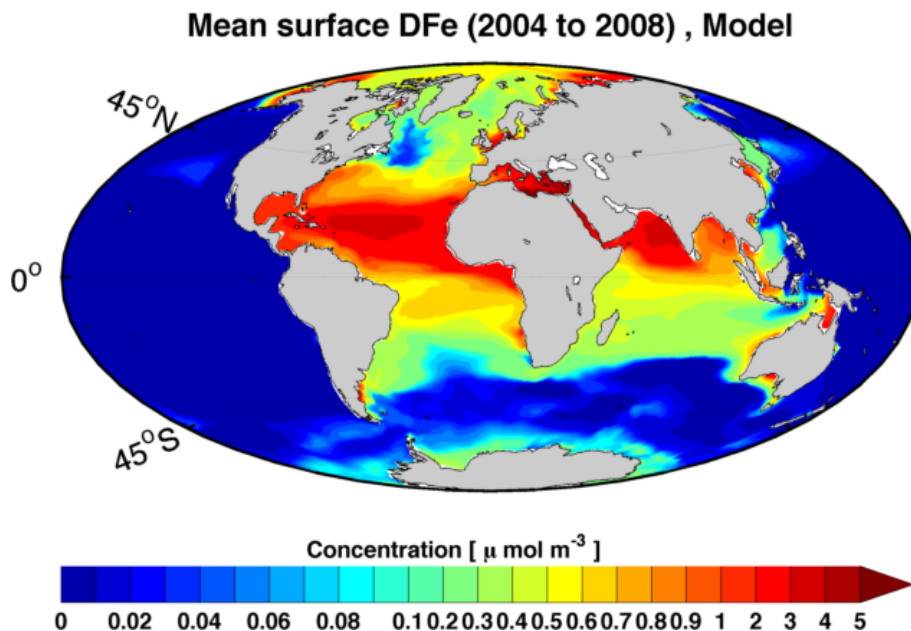
Fig. 9. Spatial distribution of the mean surface concentration of dissolved iron. Plotted to the scale used by Schneider et al. (2008).
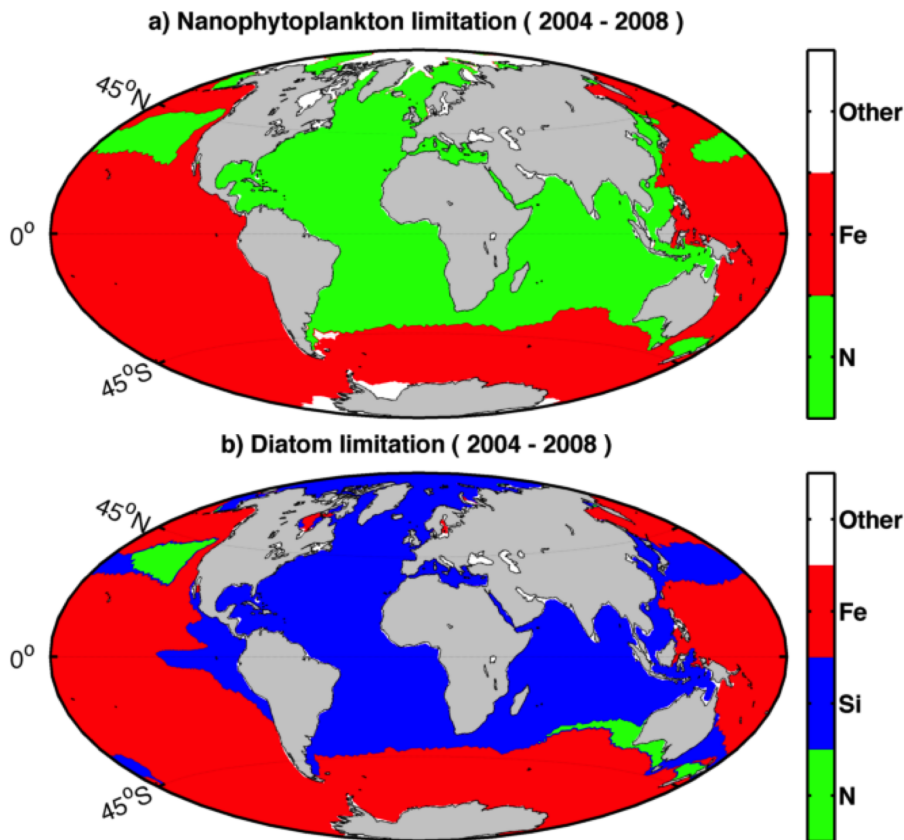
Fig. 10. Following the example of Schneider et al. (2008), the spatial distribution of the annually mean limiting nutrients in the model's surface water has been calculated. **(a)** Nanophytoplankton (Fe = 56.6 %, DIN = 40.1 % of total area). **(b)** Diatoms (Fe = 53.6 %, DIN = 2.5 % and DSi = 43.8 % of total area).
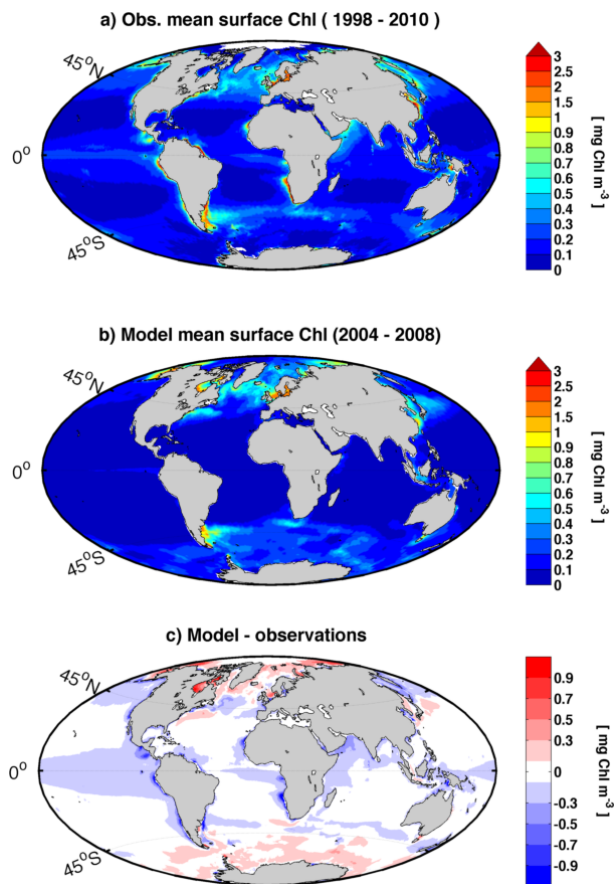
Fig. 11. Spatial distribution of mean surface concentrations of chlorophyll a plotted to the scale used by Schneider et al. (2008). **(a)** satellite-based estimate (www.globcolour.info). **(b)** Modelled. **(c)** Residual: Modelled – satellite-based estimate.
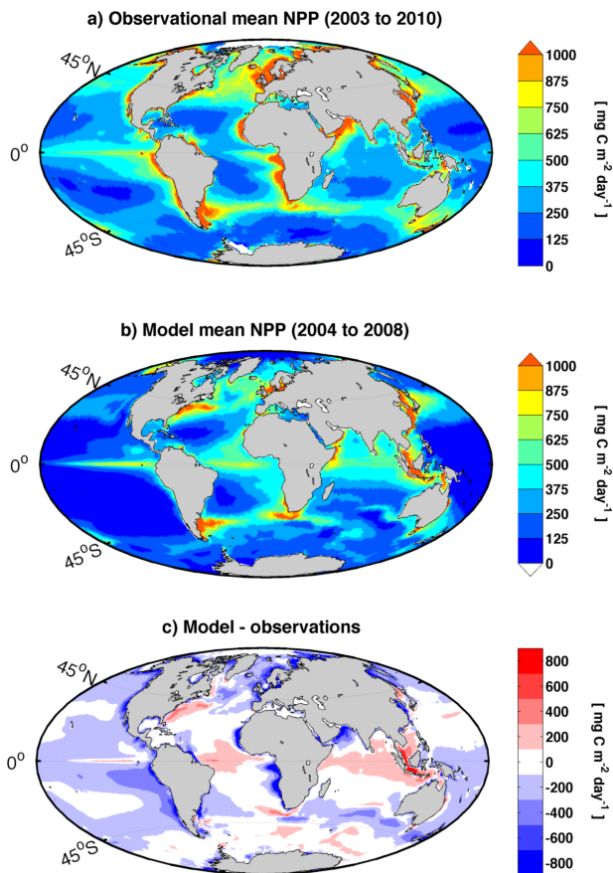
Fig. 12. Mean spatial distribution of vertically integrated net primary production plotted to the scale used by Schneider et al. (2008). **(a)** Satellite-based estimate (SeaWIFS and Behrenfeld and Falkowski, 1997). **(b)** Model. **(c)** Residual: Modelled – satellite-based estimate.

Fig. 13. Mean NPP over the year in the ocean basins depicted in Fig. 3. The correlation coefficient is written in each plot, and the statistically significant correlations (p values < 0.05) are marked with *.

a) Predicted EP (Laws) at 100 m

b) Predicted EP (Schlitzer) at 133 m

c) Modelled EP at 100 m

d) Modelled EP at 100 m

e) Model - Laws

f) Model - Schlitzer

EP [gC m^{-2} yr^{-1}]

Fig. 14. Spatial distribution of export of particulate organic matter plotted to the scale used by Moore et al. (2004). **(a)** Laws. **(b)** Schlitzer. **(c)** and **(d)** modelled (same figure). **(e)** Residual: modelled − Laws. **(f)** Residual: modelled – Schlitzer.
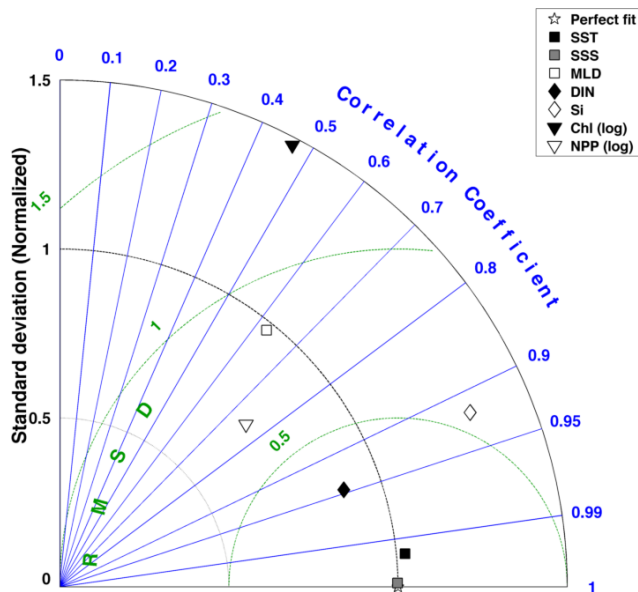
Fig. 15. Taylor diagram for the Southern Ocean south of 50° S showing correlation, normalized standard deviation and the normalized root mean square error between the spatial distribution of the model results and observed data sets, weighted by area. All values are surface values, except the mixed layer depth and the NPP, which is vertically integrated. The fields have been linearly interpolated to a 1° by 1° grid, similar to the World Ocean Atlas. Dividing with the observed standard deviation has normalized the model standard deviation and root mean square error.
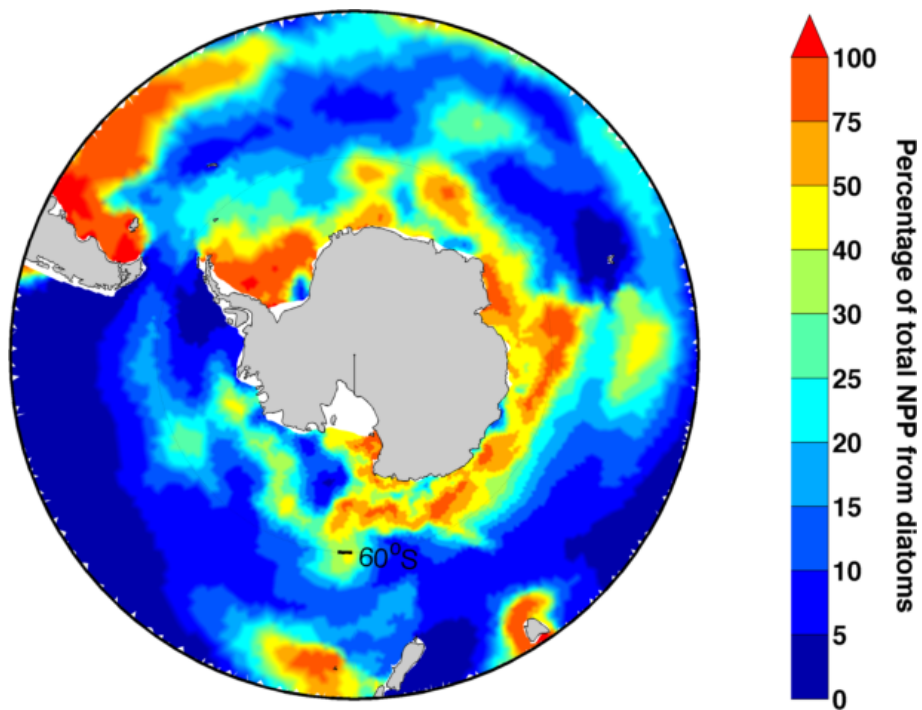
Fig. 16. Contribution of diatoms to NPP in the model.
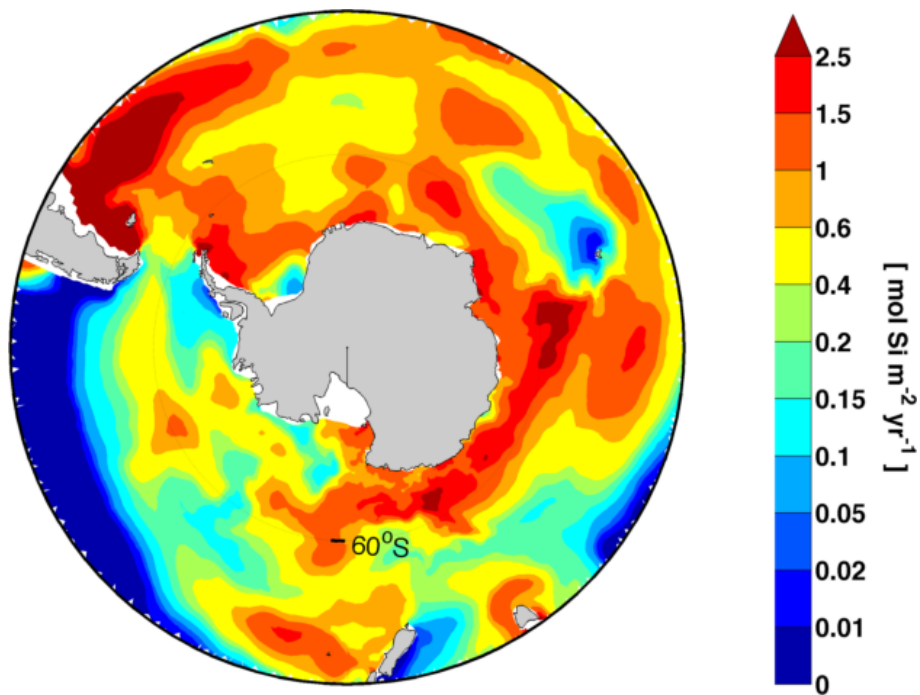
Fig. 17. Modelled export of opal across 100 m depth plotted to the scale used by Moore et al. (2004).
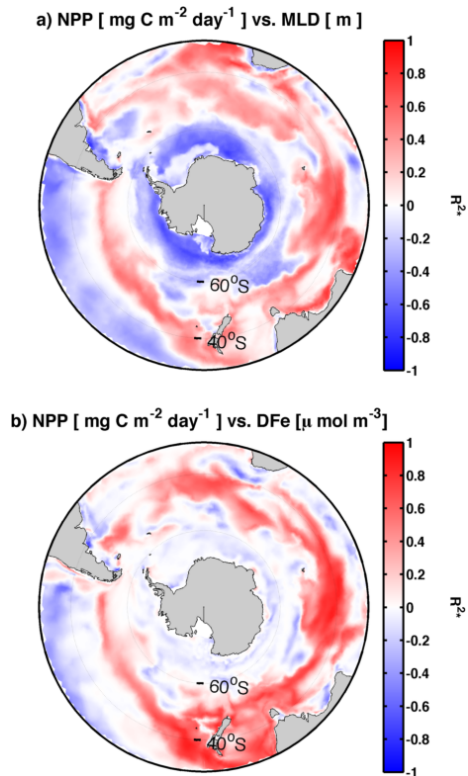
Fig. 18. Maps showing coefficients of determination for cross-correlation between model results of **(a)** NPP and DFe and **(b)** NPP and MLD. DFe has been averaged over the upper $100\,\text{m}$ of the water for the calculation. R^{2*} is defined as the temporal coefficient of correlation multiplied by the sign of the regression coefficient.
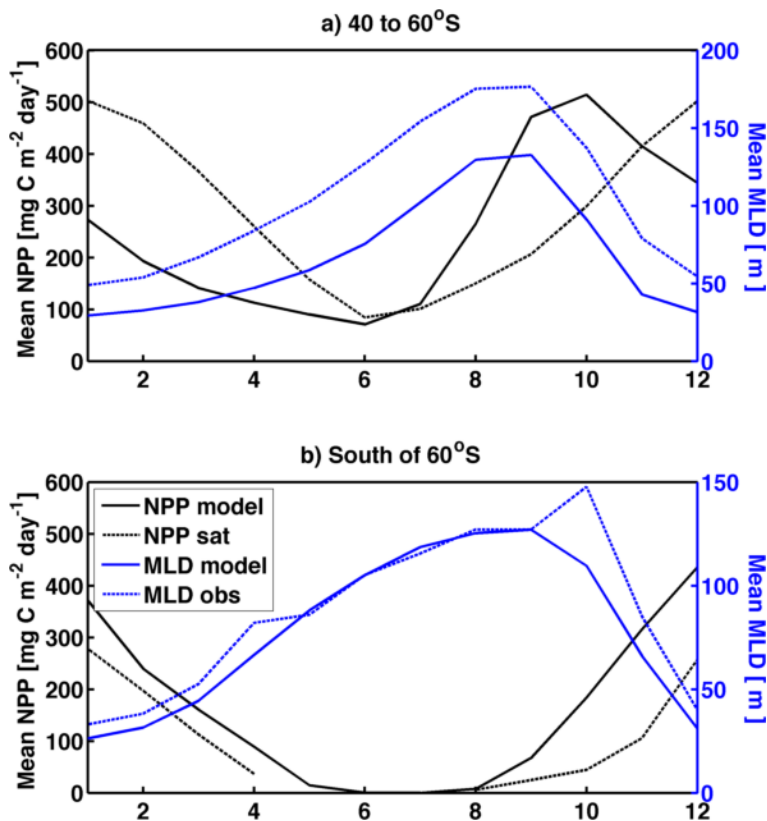
Fig. 19. Seasonal change in mean modelled and observed NPP (SeaWIFS and Behrenfeld and Falkowski, 1997) and MLD (de Boyer Montegut et al., 2004) for: **(a)** the Southern Ocean from 40 to 60° S and **(b)** south of 60° S.
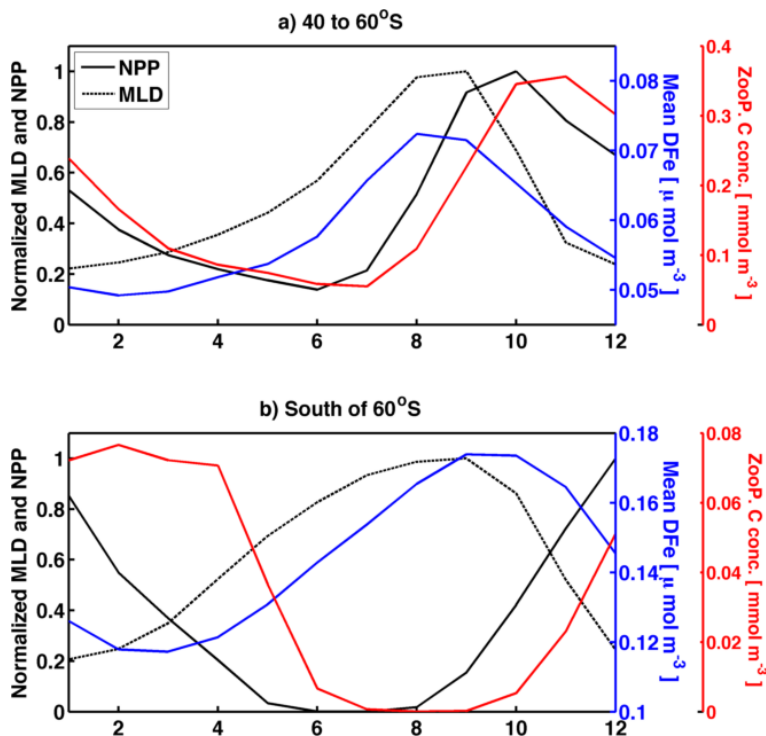
Fig. 20. Seasonal change in the modelled NPP, MLD, DFe and zooplankton concentration for: **(a)** the Southern Ocean from 40 to 60° S and **(b)** south of 60° S. DFe and zooplankton concentrations are averaged over the top 100 m of the ocean. NPP and MLD are normalized by the maximum of the monthly values.
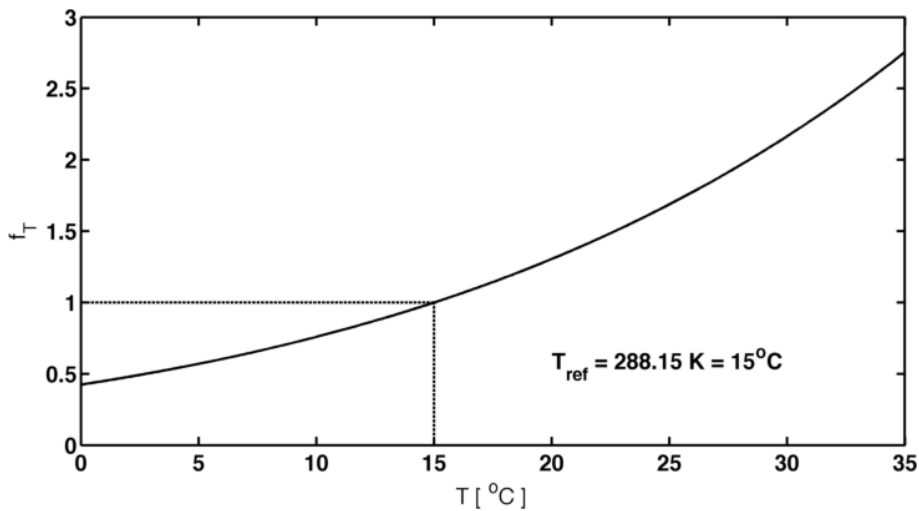
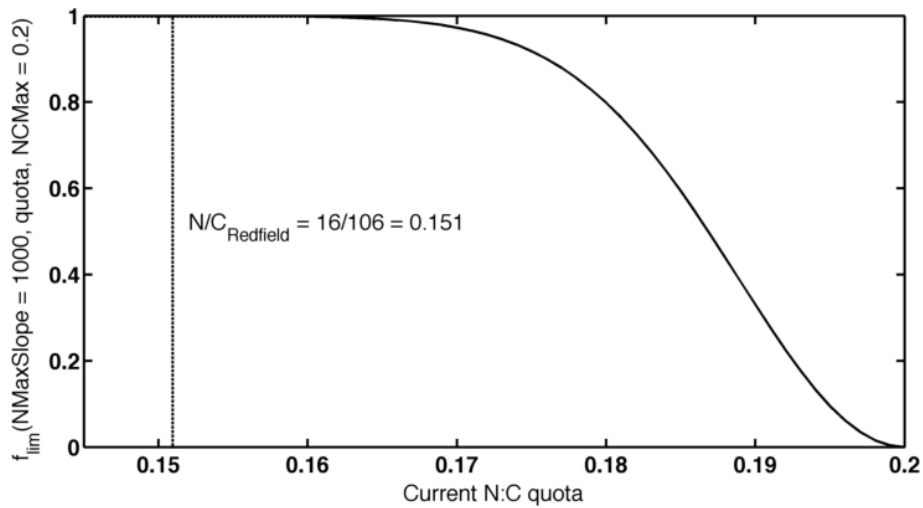**Fig. 21.** The Arrhenius function plotted with the parameters used in REcoM2.

Fig. 22. Change in limiter function $f_{\text{lim}}^{\text{N:Cmax}}$ with N : C quota.
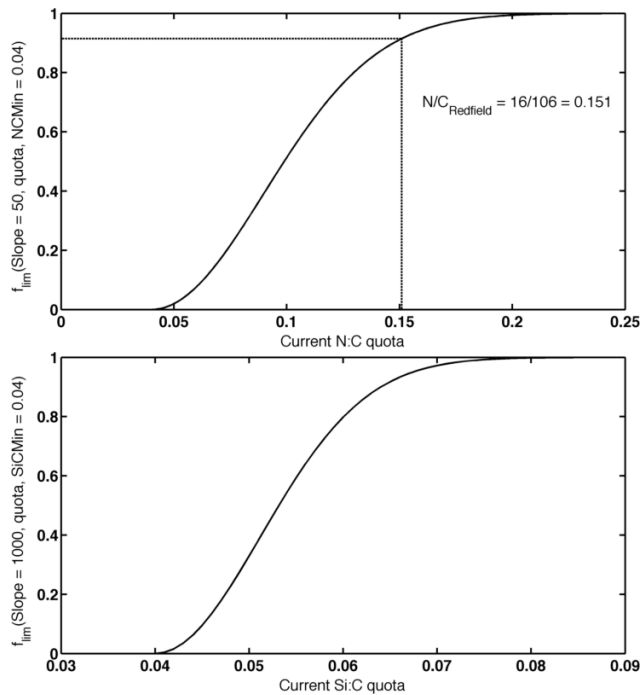
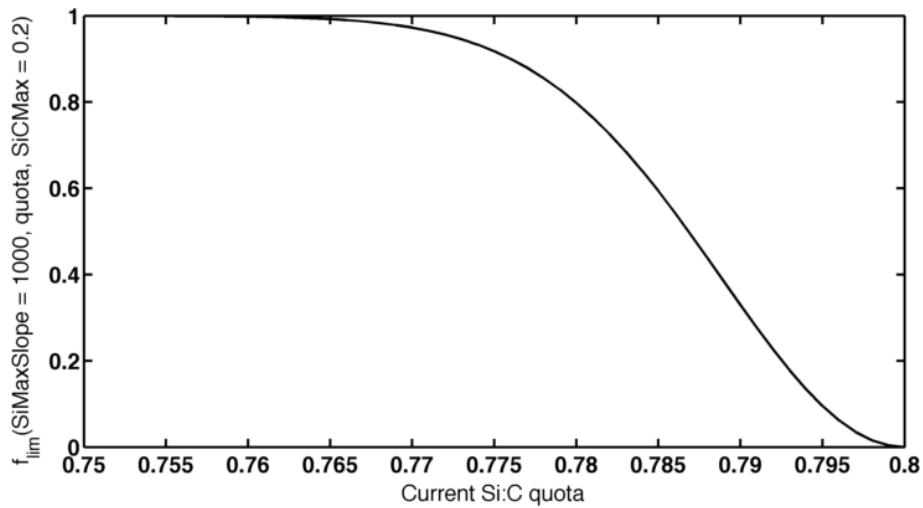**Fig. 23.** Change in the limiter function $f_{\lim}^{N:Cmin}$ with N : C quota.

Fig. 24. Change in limiter function with Si : C quota.